Mechanisms of circadian clock timing and entrainment revealed by the structure of Cryptochrome bound to Timeless

Changfan Lin[†], Shi Feng[†], Cristina C. DeOliveira and Brian R. Crane
[†]Equal Contribution

Department of Chemistry and Chemical Biology, Cornell University, Ithaca NY 14853

Circadian rhythms influence many behaviors and diseases. They arise from oscillations in gene expression caused by repressor proteins that directly inhibit transcription of their own genes. The circadian clock in flies offers a valuable model for studying these processes, wherein Timeless (TIM) plays a critical role in mediating nuclear entry of the transcriptional repressor Period (PER) and the photoreceptor Cryptochrome (CRY) entrains the clock by triggering TIM degradation in light. The cryo-EM structure of the CRY:TIM complex reveals how a light-sensing cryptochrome recognizes its target. CRY engages a continuous core of N-terminal TIM armadillo (ARM) repeats, resembling how photolyases recognize damaged DNA, and binds a C-terminal TIM helix reminiscent of the interactions between light-insensitive CRYs and their partners in mammals. The structure highlights how the CRY flavin cofactor undergoes substantial conformational changes that couple to large-scale rearrangements at the molecular interface, and how a phosphorylated segment in TIM impacts clock period by regulating the binding of importin-α and the nuclear import of TIM and PER. Moreover, the structure reveals that the TIM N-terminus inserts into the restructured CRY pocket to replace the autoinhibitory C-terminal tail released by light, thereby explaining how the LS-TIM polymorphism adapts flies to different climates.

Circadian rhythms rely on cell-autonomous molecular clocks composed of transcriptional-translational feedback loops[1,2]. In the paradigm clock of *Drosophila melanogaster* (**Figure 1a**), the transcriptional repressor proteins Period (PER) and Timeless (TIM) associate and accumulate in the cytosol before timed transport to the nucleus where they inhibit the transcription factors Clock (CLK) and Cycle (CYC)[2,3] and thereby downregulate the expression of *per*, *tim* and other clock-controlled genes[2,3] (**Figure 1a**). A cascade of TIM phosphorylation by the SHAGGY (SGG) and CK2 kinases gates nuclear entry of PER:TIM to properly time the circadian oscillator[4]. TIM co-transports PER by binding directly to the nuclear import factor importin-α1[5].

The fly clock is entrained by the flavoprotein Cryptochrome (CRY, **Figure 1a**), which binds to TIM in the light (**Figure 1b**) and directs it for proteasomal degradation[2,3]. CRYs share a flavin-binding Photolyase Homology Region (PHR) with the DNA repair enzymes photolyase (PL) but also contain a CRY C-terminal extension (CCE) that is specific for the function of a given CRY[6-8]. Type I CRYs from plants and animals sense light to reset the circadian clock; Type II CRYs from mammalians repress transcription in a light-independent manner by binding the PER proteins and directly inhibiting CLK[6,7]. In Drosophila, photoreduction of the CRY FAD to the anionic semiquinone (ASQ) by a tryptophan residue tetrad (W342, W397, W420, W394) triggers release of a C-terminal tail (CTT) helix (**Figure 1b**)[9-12,13-15]. Photoreduced CRY resets TIM levels by binding TIM and recruiting the E3 ubiquitin-ligase Jetlag (JET, **Figure 1a**)[16,17]. Recognition of TIM by CRY is hence the molecular event that sensitizes the clock to light. Although light-sensing CRYs have also been developed as powerful tools for optogenetic applications[18-20]; there is little direct structural information on how light-activated CRYs recognize their targets.

To overcome the challenge of isolating sufficient amounts of TIM (1398 residues) for structural characterization by cryo-electron microscopy (cryo-EM), we developed an insect (Drosophila S2) cell-based expression and nanobody-based affinity purification workflow for isolation of the CRY:TIM complex (264 kDa). To produce CRY:TIM, a CRY variant that lacks the 22-residue CCE[21] and therefore binds TIM constitutively[22,23] was co-transfected and expressed in S2 cells with S-TIM, the more stable of two TIM isoforms (**Supplementary Methods**). Nanobody-based affinity resin directed at a 13-residue ALFA tag allowed enrichment and elution of the complex. Complex homogeneity was further improved, and aggregation avoided by crosslinking with the lysine-specific reagent disuccinimidyl sulfoxide (DSSO) followed by SEC separation (**Extended Data Fig. 1**). Eluted samples were applied directly to glow-discharged Quantifoil® grids, vitrified, and imaged on a 200 keV Talos Arctica microscope equipped with a Gatan Quantum LS energy

filter and K3 direct electron camera. Two out of three 3D classes were refined to yield global 3.48 Å (~98 k particles) and 3.3 Å (~160 k particles) maps of the complex **(Extended Data Fig. 1 and Supplementary Table 1**). We built an atomic model based on better resolved TIM density in the 3.3 Å map (**Supplementary Movie 1**). Local resolution at the complex interface and within the body exceeds 2.5 Å.

The core of TIM revealed in the CRY:TIM complex (residues 1-248; 575-783; and 992-1128, **Figure 1b, Extended Data Fig. 2, and Supplementary Movie 1)** forms a continuous right-handed supercoil of armadillo (ARM) 3-helix repeats[24] in which two ARM domains discontinuous in sequence (ARM_1 and ARM_2, **Fig. 1c**) associate by swapping their terminal helices (**Extended Fig. 2**). TIM resembles mammalian TIM (mTIM, see below)[25] but contains an N-terminal extension that binds to CRY **(Figure 1d**). The CRY PHR comprises an N-terminal α/β domain and a C-terminal helical domain that harbors the FAD isoalloxazine ring in a central 4-helix bundle of α13-α16 (**Figure 1b,c, Extended Data Fig. 3, and Supplementary Movie 1**)[26-28]. Four helices (α8-α11) N-terminal to the helix bundle form the top of the flavin binding pocket and interact with the FAD phosphate groups and adenosine moiety (**Extended Data Fig. 3**). In this cofactor-capping region the phosphate binding loop (residues 249-263) following α8 and the protrusion motif (residues 288-306) following α10, distinguish CRYs from PLs (**Figure 1c**)[26]. The phosphate-binding loop, the protrusion motif, and the Ser-rich C-terminal lid (residues 420-446) together comprise the C-terminal coupled motif (CCM, **Figure 1c and Extended Data Fig. 3**) that changes proteolytic sensitivity when CRY becomes light activated [10].

TIM forms a discontinuous interface with CRY both at the N-terminus and C-terminus (**Figures 1b-e**). The primary CRY:TIM interface buries ~1862 $Å^2$ (49 residues) and 1807 $Å^2$ (52 residues) of solvent accessible surface area on TIM and CRY, respectively. TIM primarily binds to CRY through the first three helices of the N-terminal ARM domain (**Figure 1d,e**). ARM_1-α1 binds across CRY α17 and inserts directly into the flavin binding pocket replacing the CRY CTT (**Figures 1d, 2a, and Extended Data Fig. 4a)**. The contact is dominated by TIM ARM_1-α1-3, ARM_1-α7 and the ARM_1-α9-10 loop which mesh against elements of the CRY CCM (**Figure 1e and Extended Data Figs. 2 and 4**). At the center of the interface, Met1 and Asp2 extend out from α1 with Met1 packing against the Trp4 indole and embedding among Tyr250 and Leu251 of the CRY phosphate binding loop, Gly310 on α11, and Tyr158-Gln159 on the α5-α6 loop that extends down from the α/β domain (**Extended Data Figs. 3 and 5**). TIM Leu4 and Leu5 insert deep into the pocket

adjacent to CRY Trp314 and the FAD adenine moiety. ARM_1-α2 contacts the C-terminal lid and ARM_1-α7 contacts the protrusion motif, wherein the α10 helix lengthens to project the tip region toward the Met-rich ARM_1-α9-α10 loop at the interface periphery (**Extended Data Figs. 4c,d**).

The recognition of TIM ARM_1-a1 by CRY (**Figure 1d**) explains an evolutionary adaptation in light-sensing by flies. A *Drosophila melanogaster tim* allele (*ls-tim*) causes differential expression of two isoforms; S-TIM, which begins at the N-terminal Met residue found in the structure, and L-TIM, which extends by an additional 23 N-terminal residues owing to introduction of an alternative translational start site (**Figure 1b**)[29,30]. The frequency of *ls-tim* correlates with geographical latitude and may confer a beneficial preference for more robust rhythms and a diapause state of dormancy in climates of more variable light and cooler temperatures. L-TIM reduces interaction with CRY by yeast two-hybrid, has greater stability in fly heads, and diminishes clock responses to light [17,31]. The Met1 amino-terminus projects into a solvent channel at the interface of the two proteins that could therefore accommodate the L-TIM extension (**Figure 1d and Extended Data Fig. 6a**). However, the recognition of S-TIM by CRY through the N-terminal Met residue will be altered by the L-TIM extension (**Figure 1d)**, thereby explaining the capacity of *ls-tim* to alter fly light sensitivity.

In addition to the primary interaction between TIM ARM_1 and CRY, strong electron density for a TIM helical segment is evident among the C-terminal lid, the C-terminal end of the last CRY PHR helix (α20) and the α5-α6 loop that projects down from the α/β domain (**Figure 1e and Extended Data Fig. 3**). This TIM helix buries 496 $Å^2$ of surface area and binds at the position occupied by the residues that link α20 to the CTT in the dark-state structure, thereby supporting results from interaction studies[23] and providing further evidence that the CTT undocks from the flavin pocket upon light activation[10,12,14]. There are no obvious connections of this density to the ordered TIM ARM core and thus its sequence assignment is provisional; however, after testing many helical models and sequence registers, TIM 1163-1174 provided the most reasonable fit to the density that also adhered to the stereochemical constraints of the site (**Extended Data Fig. 7a**). To further validate this assignment, we performed the SWFTI assay (**Extended Data Fig. 8**) with TIM truncations and the CRY variant H377L that displays tight binding to TIM[13]. CRY bound TIM 1-1132 and 571-1398 similarly, but with reduced affinity compared to full-length S-TIM. TIM 1133-1398, which contains the proposed peripheral helix, alone bound to CRY-H377L (**Extended Data Fig. 8**). A known mutation of human TIM that removes the analogous C-terminal region (R1081X) causes familial advanced sleep phase by reducing interactions between mammalian TIM and

126 mCRY2[32]. Thus, although the roles of mCRY and CRY are not the same in animals and insects[2],
127 they may produce similar interactions with the otherwise disordered C-termini of their respective
128 TIM proteins. These interactions may include competition with PER because TIM 1163-1174
129 associates with CRY in a region that coincides with where mCRY binds the mammalian Period
130 proteins (**Extended Data Fig. 9a**)[33-35]

131 TIM and mTIM have a similar topology in their ARM repeats (**Extended Data Fig. 9b**) and also
132 share a C-terminal poly-(ADP-ribose) polymerase – 1 (PARP-1) binding (PAB) domain[36], which
133 includes a conserved stretch of the Timeless C region (residues 1051-1096[32]) that forms a helix
134 and loop structure (**Extended Data Fig. 9c**). However, the TIM PAB is unlikely to bind to PARP-
135 1 because it does not compose the required interface displayed by mTIM, despite high structural
136 similarity of the Drosophila and mammalian PARP-1 proteins. In fact, mTIM is more closely related
137 to the Drosophila Timeout protein (TIM-2) than to TIM itself[25,32]. Although mTIM and TIM-2 play
138 some role in circadian rhythms neither are central constituents of the core mammalian oscillator[2].
139 In contrast, mTIM and its homologs (TOF1 in yeast, SWI1 in and TIM-1 in *C. elegans*) stabilize
140 replication forks during DNA replication, pair sister chromatids and regulate S-phase
141 checkpoints[37]. Tof-1 participates in the large replisome complex in which it binds directly to dsDNA
142 (**Extended Data Fig. 9d**)[38]. Thus, details of the respective structures indicate that TIM is likely
143 functionally distinct from mTIM, Tof-1, and TIM-2, in keeping with its role in the stabilization and
144 co-transport of PER.

145 Pronounced changes in the CRY cofactor binding pocket (**Figure 2a**) involve repositioning of the
146 adenosine and ribose moieties, a large switch in the conformation of the diphosphate groups,
147 refolding of the C-terminal lid to interact with both the TIM N-terminus and ARM_1-α2 and collapse
148 of the phosphate binding loop into the flavin pocket to allow Asn253, Gln254 and Gln311 to
149 hydrogen bond with the FAD phosphates (**Extended Data Fig. 5a)**. Tyr250 and Leu251 interact
150 with the FAD pocket and make space for the top of TIM ARM_1-α3 to insert Phe58 behind the new
151 conformation of the phosphate-binding loop (**Figure 2b and Extended Data Fig. 5a**). In addition,
152 α8 tilts 20° towards the FAD diphosphates as Arg237 replaces the FAD Mg^{2+} counter ion, for
153 which no electron density is observed (**Figure 2c and Extended Data Fig. 5b**). The FAD adenine
154 ring slides 1.5 Å relative to the unbound structure, an adjustment compensated by a shift of
155 Phe318 and harboring helix α11 (**Extended Data Fig. 5b**). The 262-to-264 loop also changes
156 structure to accommodate the new diphosphate conformation and Gln311 swivels away from TIM

157 Leu4 (**Extended Data Fig. 5a,c**). A CTT-like sequence on TIM (617-626) that in isolation binds
158 light-state CRY [10] locates in the ARM core remote from the interface (**Figure 2a**).

159 The CRY:TIM complex was purified under light, although the cofactor redox state could not be
160 verified on the cryo-EM grids. Nevertheless, TIM likely stabilizes features of the light-state
161 structure. For example, the site of the light-insensitive *cryb* mutation[39], an Asp410-to-Arg381 salt
162 bridge proposed from MD simulations to restructure during light activation[40], appears to break in
163 response to the new conformation of the ribose backbone (**Figure 2d**), in keeping with light driving
164 undocking of the CTT and subsequent rearrangement of the CCM. Two conserved histidine
165 residues within the flavin pocket, His377 and His378, participate in the PL catalytic mechanism
166 and are implicated in CTT release and TIM binding[13,15,41]. In the unbound state His378 ND1
167 hydrogen bonds with O2' of the FAD ribose, but in the TIM complex, His378 tilts away from the
168 ribose hydroxyl to hydrogen bond to the TIM Leu5 carbonyl with NE2 (**Figures 2b,c and**
169 **Extended Data Fig. 5b**). Substitutions at His378 still allow CTT release, but on/off switching is
170 less robust[13,41]. Protonation of His378 NE2 is likely required for it to interact with the TIM backbone
171 carbonyl and His378 protonation may be responsive to the flavin redox state. The H377L
172 substitution substantially increases the binding affinity to TIM in both light and dark[13]. Surprisingly,
173 His377 does not contact TIM directly but rather anchors the restructured phosphate binding loop
174 by contacting several residues and hydrogen bonding to the Asn253 carbonyl (**Figure 2c**).

175 The interaction of CRY with TIM corresponds closely to how 6-4 photolyase recognizes the 6-4
176 crosslinked pyrimidine lesion in damaged DNA (**Figure 3a**). Indeed, TIM Leu4 and Leu5
177 superimpose with the crosslinked base and the TIM ARM_1-a1 polypeptide closely follows the path
178 of 5'-to-3' strand-separated DNA (**Figure 3a**)[42]. Key residues in the pocket also share identity and
179 similar positions, with the notable exception of PL Tyr306, which as a Phe in CRY contacts the
180 Leu5 side-chain. TIM and FAD also combine in CRY to mimic interactions of the FBXL3 E3 ligase
181 with apo-mCRYs for their ubiquitin mediated degradation (**Figure 3b**)[43]. Despite these similarities
182 at the primary cofactor pocket, the phosphate binding loop, protrusion motif and C-terminal lid
183 differ in both sequence and conformation among PLs, mCRYs and CRY. CRY also contains a
184 secondary pocket between its two domains that in PLs binds antenna cofactors and in mCRYs
185 mediates contacts with other clock components[6,44]. No cofactors or other constituents are found
186 within the secondary pocket of the CRY:TIM structure; however, it composes a deep cleft typical
187 of a recognition motif (**Extended Data Fig. 6b**).

188 The TIM structure provides insight into the gating of TIM:PER nuclear entry by the interaction
189 between TIM and importin-α1 (IMPα1). TIM is homologous to the β-catenins, their related family
190 members (HMP-2, p120, plakoglobin, plakophilin, and SYS-1) as well as the importin-α/β
191 karyopherins involved in nuclear transport[5,24,45]. These ARM proteins conserve a positively
192 charged groove on the concave side of their super-helical crescents where they bind extended
193 peptide chains, such as nuclear localization signals (**Figure 4a,b and Extended Data Fig. 10**)[46,47].
194 Two mutations known to block nuclear entry by reducing interactions between TIM and importin-
195 α1 (Thr90Ala and Pro92Leu; S-TIM numbering)[5] localize within the TIM groove (**Figure 4b**) but
196 do not interact with the TIM nuclear localization sequence, which rather extends in a helix along
197 the convex side of the protein (**Figure 4c**). An extended polypeptide with α-helical character
198 binds into the TIM groove adjacent to catenin-conserved Arg (84, 165) and Asn (88, 166) residues
199 (**Extended Data Fig. 10**), and Thr90/Pro92 (**Figure 4b**). Crosslinking mass spectrometry
200 revealed that TIM Lys313 and Lys328 in the disordered TIM domain (249-545) react with Lys
201 residues in the groove and toward the bottom of the crescent (**Figure 4c and Extended Data Fig.
202 10**), whereas Lys residues in other disordered regions (400-544; 784-991; 1129-1398) show little
203 crosslinking to TIM or CRY. After extensive modeling, the sequence Ser283-Thr303 was
204 provisionally assigned as the most reasonable fit to the polypeptide density (**Extended Data Fig.
205 7b**). This assignment places Asp287 and Asn291 adjacent to the conserved Asn/Arg residues
206 and occludes the Thr90 and Pro92 residues involved in importin-α1 binding (**Figure 4b**).
207
208 The Ser283-Thr303 polypeptide contains Ser286 and Ser290, which belong to the TIM-ST stretch
209 of SGG and CK2 phosphorylation sites that regulate nuclear import (TIM-ST: SGG: S268, T278;
210 CK2: T282, S286, S290; **Figures 1b and 4b**)[4]. Phosphorylation of these residues in pacemaker
211 neurons (s-LVs) increases nuclear entry rates[4]. The structure suggests that phosphorylation of
212 the TIM-ST displaces this segment from the groove to allow engagement of importin-α1 (**Figure
213 4d**). Thus, key delays that tune the clock period likely depend on the interactions of a TIM
214 autoinhibitory segment that alter upon its timed phosphorylation by circadian kinases.
215
216 The CRY:TIM structure reveals how a light-sensing cryptochrome engages its target. It also
217 provides insight into how evolutionary relationships among the component proteins comprise
218 regulatory circuits. Swapping the auxiliary CTT of CRY for the variable TIM N-terminus not only
219 sets the circadian oscillator but also tunes its light sensitivity. In this interaction, the ability of TIM
220 to serve as a peptide mimetic for a PL DNA substrate underscores how conserved structural
221 features of PLs are also utilized by CRYs. In gating its partnership with CRY, TIM shares an

222 autoinhibitory mechanism that resembles that which regulates importin-α[47-49]. The striking
223 changes in FAD geometry that couple to CRY conformational rearrangement and TIM binding
224 were unexpected. These new insights raise questions as to whether other flavoprotein light-
225 sensors share similar mechanisms to convey light or redox signals from their cofactors.
226

227 ## References
228

229 1 Takahashi, J. S. Transcriptional architecture of the mammalian circadian clock. *Nature*
230 *Reviews Genetics* **18**, 164-179 (2017).

231 2 Crane, B. R. & Young, M. W. interactive features of proteins composing eukaryotic
232 circadian clocks. *Ann. Rev. Biochem.* **83** (2014).

233 3 Foley, L. E. & Emery, P. Drosophila Cryptochrome: Variations in blue. *Journal of*
234 *Biological Rhythms* **35**, 16-27 (2020).

235 4 Top, D., Harms, E., Syed, S., Adams, E. L. & Saez, L. GSK-3 and CK2 kinases
236 converge on Timeless to regulate the master clock. *Cell Reports* **16**, 357-367 (2016).

237 5 Jang, A. R., Moravcevic, K., Saez, L., Young, M. W. & Sehgal, A. Drosophila TIM binds
238 Importin α1, and acts as an adapter to transport PER to the nucleus. *Plos Genetics* **11**
239 (2015).

240 6 Chaves, I. *et al.* The cryptochromes: blue light photoreceptors in plants and animals.
241 *Annual review of plant biology* **62**, 335-364 (2011).

242 7 Ozturk, N. Phylogenetic and functional classification of the photolyase/cryptochrome
243 family. *Photochemistry and Photobiology* **93**, 104-111 (2017).

244 8 Parico, G. C. G. *et al.* The human CRY1 tail controls circadian timing by regulating its
245 association with CLOCK:BMAL1. *Proc. Natl. Acad. Sci. US.* **117**, 27971-27979 (2020).

246 9 Berndt, A. *et al.* A novel photoreaction mechanism for the circadian blue light
247 photoreceptor Drosophila cryptochrome. *J Biol Chem* **282**, 13011-13021 (2007).

248 10 Vaidya, A. T. *et al.* Flavin reduction activates Drosophila cryptochrome. *Proc Natl Acad*
249 *Sci USA* **110**, 20455-20460 (2013).

250 11 Ozturk, N., Selby, C.P., Annayev, Y., Zhong, D., Sancar, A. Reaction Mechanism of
251 Drosopila cryptochrome. *Proc Natl Acad Sci USA* **108**, 516-521 (2011).

252 12 Lin, C. F., Top, D., Manahan, C. C., Young, M. W. & Crane, B. R. Circadian clock activity
253 of cryptochrome relies on tryptophan-mediated photoreduction. *Proc. Natl. Acad. Sci.*
254 *USA* **115**, 3822-3827 (2018).

255 13 Lin, C., Schneps, C. M., Chandrasekaran, S., Ganguly, A. & Crane, B. R. Mechanistic
256 insight into light-dependent recognition of Timeless by Drosophila Cryptochrome.
257 *Structure* doi: 10.1016/j.str.2022.03.010 (2022).

14 Chandrasekaran, S. *et al.* Tuning flavin environment to detect and control light-induced conformational switching in Drosophila cryptochrome. *Communications biology* **4**, 1-12 (2021).

15 Ganguly, A. *et al.* Changes in active site histidine hydrogen bonding trigger cryptochrome activation. *Proc. Natl. Acad. Sci. U. S. A.* **113**, 10073-10078 (2016).

16 Koh, K., Zheng, X. Z. & Sehgal, A. JETLAG resets the Drosophila circadian clock by promoting light-induced degradation of TIMELESS. *Science* **312**, 1809-1812 (2006).

17 Peschel, N., Chen, K. F., Szabo, G. & Stanewsky, R. Light-dependent interactions between the Drosophila circadian clock factors cryptochrome, jetlag, and timeless. *Current Biology* **19**, 241-247 (2009).

18 Zhou, X. X. *et al.* A single-chain photoswitchable CRISPR-Cas9 architecture for light-inducible gene editing and transcription. *ACS Chem Biol* **13**, 443-448 (2018).

19 Yu, D. *et al.* Optogenetic activation of intracellular antibodies for direct modulation of endogenous proteins. *Nat Methods* **16**, 1095-1100 (2019).

20 Gil, A. A. *et al.* Optogenetic control of protein binding using light-switchable nanobodies. *Nat Commun* **11**, 4044 (2020).

21 Busza, A., Emery-Le, M., Rosbash, M. & Emery, P. Roles of the two Drosophila Cryptochrome structural domains in circadian photoreception. *Science* **304**, 1503-1506 (2004).

22 Dissel, S. *et al.* A constitutively active cryptochrome in Drosophila melanogaster. *Nat. Neurosci.* **7**, 834-840 (2004).

23 Hemsley, M. J. *et al.* Linear motifs in the C-terminus of D-melanogaster cryptochrome. *Biochemical and Biophysical Research Communications* **355**, 531-537 (2007).

24 Vodovar, N., Clayton, J. D., Costa, R., Odell, M. & Kyriacou, C. P. The Drosophila clock protein Timeless is a member of the Arm/HEAT family. *Current Biology* **12**, R610-R611 (2002).

25 Holzer, S. *et al.* Crystal structure of the N-terminal domain of human Timeless and its interaction with Tipin. *Nucleic Acids Research* **45**, 5555-5563 (2017).

26 Zoltowski, B. D. *et al.* Structure of full-length Drosophila cryptochrome. *Nature* **480**, 396-399 (2011).

27 Levy, C. *et al.* Updated structure of Drosophila cryptochrome. *Nature* **495**, E3-4 (2013).

28 Czarna, A. *et al.* Structures of Drosophila cryptochrome and mouse cryptochrome1 provide insight into circadian function. *Cell* **153**, 1394-1405 (2013).

29 Tauber, E. *et al.* Natural selection favors a newly derived timeless allele in Drosophila melanogaster. *Science* **316**, 1895-1898 (2007).

30 Deppisch, P. *et al.* Adaptation of Drosophila melanogaster to long photoperiods of high-latitude summers is facilitated by the ls-timeless allele. *J. Biol. Rhythms* **37**, 185-201 (2022).

31 Sandrelli, F. *et al.* A molecular basis for natural selection at the timeless locus in Drosophila melanogaster. *Science* **316**, 1898-1900 (2007).

32 Kurien, P. *et al.* TIMELESS mutation alters phase responsiveness and causes advanced sleep phase. *Proc. Natl. Acad. Sci. USA* **116**, 12045-12053 (2019).

33 Schmalen, I. *et al.* Interaction of circadian clock proteins CRY1 and PER2 Is modulated by zinc binding and disulfide bond formation. *Cell* **157**, 1203-1215 (2014).

34 Fribourgh, J. L. *et al.* Dynamics at the serine loop underlie differential affinity of cryptochromes for CLOCK:BMAL1 to control circadian timing. *Elife* **9** (2020).

35 Nangle, S. N. *et al.* Molecular assembly of the period-cryptochrome circadian transcriptional repressor complex. *Elife* **3** (2014).

36 Xie, S. *et al.* Timeless interacts with PARP-1 to promote homologous recombination repair. *Molecular Cell* **60**, 163-176 (2015).

37 Engelen, E. *et al.* Mammalian Timeless Is Involved in period determination and DNA damage-dependent phase advancing of the circadian clock. *PLoS One* **8** (2013).

38 Baretic, D. *et al.* Cryo-EM Structure of the fork protection complex bound to CMG at a replication fork. *Molecular Cell* **78**, 926-+ (2020).

39 Stanewsky, R. *et al.* The *cry(b)* mutation identifies cryptochrome as a circadian photoreceptor in Drosophila. *Cell* **95**, 681-692 (1998).

40 Wang, Y. J., Veglia, G., Zhong, D. P. & Gao, J. L. Activation mechanism of Drosophila cryptochrome through an allosteric switch. *Science Advances* **7** (2021).

41 Berntsson, O. *et al.* Photoactivation of Drosophila melanogaster cryptochrome through sequential conformational transitions. *Science Advances* **5** (2019).

42 Glas, A. F., Schneider, S., Maul, M. J., Hennecke, U. & Carell, T. Crystal structure of the T(6-4)C lesion in complex with a (6-4) DNA photolyase and repair of UV-induced (6-4) and dewar photolesions. *Chemistry-a European Journal* **15**, 10387-10396 (2009).

43 Nangle, S., Xing, W. M. & Zheng, N. Crystal structure of mammalian cryptochrome in complex with a small molecule competitor of its ubiquitin ligase. *Cell Research* **23**, 1417-1419 (2013).

44 Rosensweig, C. *et al.* An evolutionary hotspot defines functional differences between cryptochromes. *Nature Communications* **9** (2018).

45 Tewari, R., Bailes, E., Bunting, K. A. & Coates, J. C. Armadillo-repeat protein functions: questions for little creatures. *Trends in Cell Biology* **20**, 470-481 (2010).

46 Choi, H. J. *et al.* A conserved phosphorylation switch controls the interaction between cadherin and β-catenin In Vitro and In Vivo. *Developmental Cell* **33**, 82-93 (2015).

47 Goldfarb, D. S., Corbett, A. H., Mason, D. A., Harreman, M. T. & Adam, S. A. Importin-α: a multipurpose nuclear-transport receptor. *Trends in Cell Biology* **14**, 505-514 (2004).

48 Catimel, B. *et al.* Biophysical characterization of interactions involving importin-alpha during nuclear import. *Journal of Biological Chemistry* **276**, 34189-34198 (2001).

49 Harreman, M. T., Hodel, M. R., Fanara, P., Hodel, A. E. & Corbett, A. H. The auto-inhibitory function of importin-α is essential in Vivo. *Journal of Biological Chemistry* **278**, 5854-5863 (2003).

50 Holm, L. & Laakso, L. M. Dali server update. *Nucleic Acids Research* **44**, W351-W355 (2016).

Figure 1. Cryo-EM structure of the CRY:TIM complex. (**a**) Drosophila Cryptochrome (CRY) entrains the circadian clock by initiating degradation of Timeless (TIM) in light. Jetlag (JET), Period (PER), Doubletime (DB), Cycle (CYC), Clock (CLK) and Importin-α1 (IMPα1) compose the core circadian oscillator. (**b**) CRY:TIM docked into the electron density map. Dark-state CRY shown at the bottom (grey, PDB ID: 4GU5). (**c**) Domain arrangements and key regions of CRY and TIM. Features of TIM: CRY-binding domains (CRY-BD1, 1-234, CRY-BD2, 1133-1398), serine/threonine-rich region (ST, 270-290) with key phosphorylation sites starred (S274, T278, T282, S286 and S290), ARM1 (1-248), ARM2 (578-866), nuclear localization sequence (NLS, 545-578), Parp-1 binding domain (PAB, 986-1142; TIM-C, 1051-1096), 23 residue L-TIM extension (L, (23aa)), disordered regions are dashed. Features of CRY: Phosphate binding loop (PL, 249-263), Protrusion motif (PM, 288-306), C-terminal lid (CL, 420-446), C-terminal tail (CTT, 519-542, absent in CRYΔ). (**d**) N-terminus of TIM inserts into the primary flavin binding pocket. 2.4 Å resolution local electron density is shown with notable hydrogen bonds (yellow dashes) and hydrophobic contacts (green circle). (**e**) Interface between CRY and TIM (blue shaded area), TIM groove peptide (in navy blue) and peripheral helix (fitted with 1163-1174 putatively, blue). Inset shows the interactions between TIM 1163-1174 and CRY superimposed with electron density.

Figure 2. Conformational changes of FAD to the CRY C-terminal coupled motif upon binding TIM. (**a**) CRY:TIM (CRY, yellow; TIM, blue) in superposition with dark-state CRY. The N-terminus of TIM replaces the CRY CTT (red), as depicted in the schematic below. Structural elements designated as in **Figure 1**. (**b**) The phosphate binding loop (dark pink) collapses into the flavin pocket and N253 and E254 hydrogen bond (yellow dashes) with the FAD diphosphate

363 conformation (red, orange) that differs substantially from that of the dark state (white bonds). (**c**)
364 R237 replaces the Mg^{2+} counter ion and H377 anchors the new position of the loop. The D410-
365 R381 salt bridge (top) appears to break in response to the new conformation of the ribose
366 backbone (bottom). Reduced side-chain density of R381 suggests increased flexibility in the TIM
367 complex.
368
369 **Figure 3. Conservation of recognition modes by CRY family members.** (**a**) The interaction of
370 CRY with TIM corresponds closely to how 6-4 photolyase recognizes the 6-4 pyrimidine lesion in
371 damaged DNA (PDB ID:3CVU). TIM Leu4 and Leu5 superimpose on the crosslinked bases and
372 the TIM ARM1- α1 polypeptide closely follows the path of 5'-to-3' strand-separated DNA. (**b**) The
373 TIM and FAD contacts of CRY mimic the interaction of apo-mCRY with the C-terminus of the
374 FBXL3 E3 ligase (PDB ID: 4I6J).
375
376 **Figure 4. A structural basis for regulation of TIM nuclear entry.** (**a**) Electron density (dark
377 blue) for an extended polypeptide resides within a groove wherein members of the β-catenin and
378 α-importin proteins bind their target sequences. (**b**) The TIM groove peptide density shown with
379 the sequence assignment S283-T303. The peptide interacts with β-catenin-conserved Asn and
380 Arg residues and buries residues important for importin-α1 binding (T90 and P92). (**c**) DSSO-
381 mediated lysine crosslinking patterns of disordered residues K313 and K238 shown on the TIM
382 structure. K313 and K328 produce a pattern of crosslinking that localizes them to a position
383 consistent with placement of the S283-T303 groove peptide. The TIM NLS lies in a helix adjacent
384 to the groove but does not occlude T90 and P92. (**d**) Schematic of proposed nuclear entry
385 mechanism of TIM. Phosphorylation of the TIM-ST region by SGG and CK2 releases the ST
386 region from TIM groove to expose TIM T90 and P92. Importin-α1 recognizes TIM by binding
387 adjacent to Thr90 and Pro92, while also binding the TIM NLS within a structurally analogous ARM
388 groove of its own.
389
390 ## Methods
391 ### Cloning
392 All DNA constructs (shown above) were built by a modified Gibson assembly method and Q5
393 polymerase-based mutagenesis with home-made reaction mixture, as reported previously[51].
394
395 ### Transient co-transfection of S2 cells

396 S2 cells were maintained at 27 °C in 90% Schneider's Drosophila Medium (Cat# 21720024,
397 ThermoFisher) suppled with 10% heat-inactivated Fetal Bovine Serum (FBS, Cat# F4135, sigma),
398 as reported previously[51]. pAC5.1 vectors of CLIP-CRYΔ and TIM-SNAP-HA-ALFA were delivered
399 into S2 cells using the TransIT-Insect Transfection Reagent (Cat# MIR6100, Mirus) following a
400 modified version of the manufacturer's instruction. Briefly, about twenty 100 mm culture dishes
401 (Cat# 353003, Corning) with $1000x10^4$ cells in 10 ml fresh growth medium were prepared on day
402 1. About 20 hours later, 10 µg DNA in total (CRYΔ: TIM mass ratio 1:1) were transfected by the
403 TransIT-Insect reagent in each 100 mm dish. 72 hours after transfection, cells were harvested by
404 centrifugation with 500 × g for 5 minutes at room temperature, washed once with chilled PBS and
405 then stored at -80 °C until lysis.
406
407 **Nanobody-based affinity purification of the CRY:TIM complex**
408 Two cycles of freeze-thaw were used to lyse the S2 cells as follows: S2 cell pellets from 200 ml
409 of culture were resuspended with 16 ml lysis buffer (50 mM Tris, pH 8, NaCl 150 mM, 20% glycerol,
410 1x protease inhibitor (Cat# A32965, ThermoFisher)) and flash frozen in liquid nitrogen. The
411 sample was then quickly thawed as 800 ul aliquots in a room temperature water bath. The lysate
412 aliquot was resupended (without vortexing) and the freeze-thaw cycle repeated. 100 U/ml
413 benzonase (sc-202391, Santa Cruz Biotechnology) was added to the sample and incubated at
414 4 °C for 45 min to remove DNA/RNA contamination. The cell lysate was spun at 20000 x g for 20
415 minutes at 4 °C and further filtered with a 0.45 micron PVDF syringe filter (Cat# SLHV033NB,
416 Millipore Sigma). 160 µL settled ALFA resin (pre-washed with lysis buffer A) was incubated with
417 the cell lysate at 4 °C for 1 h on an end-to-end rotator (Cat# 88881001, ThermoFisher scientific).
418 The slurry was transferred to a 15 ml falcon tube, centrifuged at 1000 x g for 1 min and wash the
419 resin with 7 mL wash buffer (HEPES 50 mM, pH 7.9, NaCl 150 mM, 10% glycerol). This process
420 was repeated 3 times. Then the resin was resuspended in 1 mL wash buffer and split into two
421 and applied to separate spin columns (Cat# 6572, BioVision), with 80 µL resin applied to each
422 column. The spin columns were washed 4 times with 500 ul wash buffer. 500 µL elution buffer
423 (wash buffer with 200 uM ALFA peptide) was added to 80 µL resin in each spin column and
424 incubated in the cold room for 20 min on an end-to-end rotator. The columns were spun at 1000
425 x g for 1 min to collect the elution. The elution was repeated 3 times and all of the elutions were
426 then combined (3 mL in total).
427
428 **DSSO crosslinking coupled with SEC**

429 The elution was concentrated to about 70 to 80 μL (while maintaining the final protein
430 concentration at less than 2 mg/mL to ensure efficient crosslinking) with a 30 kDa vivaspin
431 concentrator (Cat# 28932235, Cytiva). 50 mM stock solution of DSSO was prepared in dimethyl
432 sulfoxide (DMSO) following the manufacture's instructions. DSSO was added to the elution
433 sample to a final concentration of 1 mM and incubated at room temperature for 45 minutes,
434 followed by quenching for 5 min at room temperature with addition of 1 M Tris buffer (pH 8) to
435 produce a final concentration of 20 mM Tris. The crosslinked complex was concentrated by 50
436 kDa vivaspin (Cat# 28932236, Cytiva) and purified by a Superose SEC column 6 10/300 (Cat#
437 29091596, Cytiva) or 3.2/300 (Cat# 29091598, Cytiva). The protein complex was eluted in SEC
438 buffer (20 mM HEPES, pH 7.9, 150 mM NaCl) and concentrated to ~40 μL by a 50 kDa cutoff
439 vivaspin concentrator.
440
441 **Cross-Linking Mass Spectrometry (XL-MS)**
442 SEC-purified crosslinked product was mixed with 4x Laemmli Sample Buffer (Cat# 1610747,
443 BioRad) and 2.5% 2-mercaptoethanol (BME, Cat# 1610710, BioRad) and then boiled for 6 min.
444 The sample was then loaded on an SDS-PAGE gel and stained with QC Colloidal Coomassie
445 Stain (Cat #1610803, BioRad). The band of the complex (~ 20 ug protein sample) was cut out
446 and prepared for MS-MS analysis of crosslinked peptides as previously reported[52] and described
447 below.
448
449 **In-gel digestion of SDS gel bands**
450 The protein band (~ 20 µg protein) was sliced into ~1 mm cubes. The excised gel pieces were
451 washed consecutively with 400 µL deionized water followed by 50 mM ammonium bicarbonate,
452 50% acetonitrile and finally 100% acetonitrile. The dehydrated gel pieces were reduced with 200
453 µL of 10 mM DTT in 100 mM ammonium bicarbonate for 45 min at 56 °C, followed by alkylation
454 with 200 µL of 55 mM iodoacetamide in 100 mM ammonium bicarbonate at room temperature in
455 the dark for 45 min. Wash steps were repeated as described above. The gel was then dried and
456 rehydrated with 100 µL LysC at 10 ng/µL in 50 mM ammonium bicarbonate containing 10%
457 acetonitrile (ACN) and incubated at 37 °C for 3 h. After the 3 h incubation, 30 µL Trypsin at 43
458 ug/uL in 50 mM ammonium bicarbonate was added and the sample was continued to incubate at
459 37 °C for 18 h. The digested peptides were extracted from the gel twice with 200 µL of 50%
460 acetonitrile containing 5% formic acid and once with 200 µL of 75% acetonitrile containing 5%
461 formic acid. Extractions from each sample were pooled together and then divided equally in half.
462 One half was then filtered with 0.22 µm spin filter (Costar Spin-X from Corning), dried to dryness

463 in the speed vacuum and analyzed as LysC/Trypsin digests. The second half was dried to
464 dryness in the speed vacuum then reconstituted with 30 µL GluC at 33 ng/µL in 50mM ammonium
465 bicarbonate (pH 7.9), incubated at 37 °C for 18 h. After incubation, formic acid was added to stop
466 enzyme reaction. The digests were filtered with 0.22 µm spin filter, dried to dryness in the speed
467 vacuum and analyzed as LysC/Trypsin/GluC digests. Each sample was reconstituted in 0.5%
468 formic acid prior to LC- MS/MS analysis.
469
470 **Crosslinks identification by nanoLC-MS/MS**
471 The digested product was characterized by NanoLC-MS/MS analysis at the Cornell Biotechnology
472 Resource Center. The analysis was carried out using an Orbitrap Fusion™ Tribrid™ (Thermo-
473 Fisher Scientific, San Jose, CA) mass spectrometer equipped with a nanospray Flex Ion Source,
474 and coupled with a Dionex UltiMate 3000 RSLCnano system (Thermo, Sunnyvale, CA). Each
475 sample was loaded onto a nano Viper PepMap C18 trapping column (5 µm, 100 µm × 20 mm,
476 100 Å, Thermo Fisher Scientific) at 20 µL/min flow rate for rapid sample loading. After 3 minutes,
477 the valve switched to allow peptides to be separated on an Acclaim PepMap C18 nano column
478 (2 µm, 75 µm x 25 cm, Thermo Fisher Scientific) at 35 °C in a 90 min gradient of 5% to 40% buffer
479 B (98% ACN with 0.1% formic acid) at 300 nL/min. The Orbitrap Fusion was operated in positive
480 ion mode with nano spray voltage set at 1.7 kV and source temperature at 275 °C. External
481 calibrations for Fourier transform, ion-trap and quadrupole mass analyzers were performed prior
482 to the analysis. Samples were analyzed using the CID-MS^2-MS^3 workflow, in which MS scan
483 range was set to 375–1500 m/z and the resolution was set to 60,000. Precursor ions with charge
484 states 3-8 were selected for CID MS^2 acquisitions in Orbitrap analyzer with a resolution of 30,000
485 and an AGC target of 5 $\times 10^4$. The precursor isolation width was 1.6 m/z and the maximum
486 injection time was 100 ms. The CID MS^2 normalized collision energy was set to 25%. Targeted
487 mass-difference triggered HCD-MS^3 spectra were acquired in the ion trap with AGC target of 1
488 $\times 10^4$. When a unique mass difference (Δ=31.9721 Da) was observed in CID-MS^2 spectra for ions
489 with a single charge and multiple charges, the HCD collision energy at 38% and 28% was used
490 respectively, for the subsequent MS^3 scans. All data were acquired under Xcalibur 4.3 operation
491 software and Orbitrap Fusion Tune application v3.4 (Thermo-Fisher Scientific).
492
493 **MS Data analysis**
494 All MS, MS^2 and MS^3 raw spectra from each sample were searched using Proteome Discoverer
495 2.4 (Thermo-Fisher Scientific, San Jose, CA) with XlinkX v2.0 algorithm for identification of
496 crosslinked peptides. The search parameters were as follow: four missed cleavage for either

497 double digestion or triple digestion with fixed carbamidomethyl modification of cysteine, variable
498 modifications of methionine oxidation, asparagine and glutamine deamidation, protein N-terminal
499 acetylation. The peptide mass tolerance was 10 ppm, and MS^2 and MS^3 fragment mass tolerance
500 was 20 ppm and 0.6 Da, respectively. The *Drosophila melanogaster* database with added
501 targeted protein sequences was used for PD 2.4 database search with 1% FDR for report of
502 crosslink results. Identified crosslinked peptides were filtered for Max. XlinkX Score > 40
503 containing at least two identified MS^3 spectra for each pair of crosslinked peptides. Search Results
504 were exported by the software as a spreadsheet. The crosslinked peptides were analyzed by
505 xiNET for generating the viewer of inter or inner crosslinks between two target proteins.
506
507 **SWFTI assay**
508 S2 cells were co-transfected as described above with pAC 5.1 vectors of CLIP-CRY-377L and
509 TIM-SNAP-HA-ALFA variants at a mass ratio of 3:1. The pulldown assay was carried out as
510 follows, similar to that previously described[51]. 5 mL of S2 cell pellets were lysed with 400 µL lysis
511 buffer containing non-ionic detergent (50 mM Tris buffer, pH 8, 150 mM NaCl, 1% IGEPAL CA-
512 630 (Cat# I8896, Sigma Aldrich), 10% glycerol and 1x protease inhibitor (Cat# A32965,
513 ThermoFisher)) was added to cell pellets harvested from 5 mL cells. EDTA was omitted to avoid
514 disturbing SNAP/CLIP dye labeling. All buffer pHs were adjusted at the working temperature. After
515 cells were incubated with lysis buffer on ice for 30 mins (flicking the tube every 10 min to avoid
516 vortexing), cell debris was removed by spinning at 15,000 × g for 15 minutes at 4°C.
517 To label the lysate sample with SNAP/CLIP dyes, 1 part of lysate was diluted with 2 parts of
518 labeling buffer (50 mM Tris buffer, pH 8, 150 mM NaCl, 10% glycerol) to decrease the
519 concentration of non-ionic detergent to less than 0.5%, as recommended by the manufacturer
520 (New England Biolabs). Then 27 µL of diluted lysate was mixed with 1 µL of 0.1 mM SNAP dye
521 (Cat# S9102S, SNAP-Cell 647-SiR), 1 ul 0.1 mM CLIP dye (Cat# S9217S, CLIP-Cell 505) and 1
522 ul 30 mM DTT and incubated in the dark at room temperature for 1 hour. 10 uL 4x Laemmli sample
523 buffer (Cat# 1610747, BioRad) and 1.5 µL 2-mercaptoethanol (BME) was added to the 30 µL mix,
524 boiled at 95 °C for 5 minutes. After labeling with the SNAP/CLIP substrate, the sample was
525 protected from bright light to avoid photobleaching. 20 µL of the sample was loaded on a gradient
526 stain-free gel (Cat# 4568095, BioRad) to perform SDS-PAGE. The result was imaged with
527 Chemidoc (BioRad) and quantified by image lab software (BioRad).
528
529 To label CRY and TIM on the affinity resin, ~350 µL cell lysate was mixed with 10 µL pre-washed
530 magnetic HA resin slurry (Cat# 88836, ThermoFisher) and incubated on an end-to-end rotator

531 overnight at 4 °C. The dark sample was covered by foil and kept in the dark. Next day, the resin
532 was washed with room temperature 500 µL TBS-T (20 mM Tris buffer, pH 7.6, 150 mM NaCl,
533 0.05% Tween-20) four times. Then HA resin was resuspended in 27 µL labeling buffer, 1 µL 0.1
534 mM SNAP dye, 1 µL 0.1 mM CLIP dye and 1 µL 30 mM DTT. The tube was incubated in the dark
535 on an end-to-end rotator at room temperature for one hour. Subsequently, 10 µL 4x Laemelli
536 sample buffer and 1.5 µL BME were added to the 30 µL resin mix. The tube was boiled at 95 °C
537 for 10 minutes to denature and elute CRY and TIM from HA resin. SDS-PAGE and imaging were
538 performed the same as above. Effective KD values were calculated as described elsewhere[51].
539
540 **Negative Stain Electron Microscopy**
541 Initial CRY:TIM samples were screened by negative-stain. Formvar/carbon 200 mesh copper
542 grids (Electron Microscopy Sciences) was plasma cleaned by the GloQube glow discharge
543 system (Electron Microscopy Sciences). Ten µL of 0.05 mg/ml CRY:TIM solution was applied
544 onto the grid, incubated for 30 seconds, and the excess solution was blotted with filter paper. 10
545 µl of 2% uranyl acetate was then applied to the grid twice for 30-second incubation followed by
546 blotting. The grid was air-dried for 5 minutes and visualized by Philips Morgagni 268 Transmission
547 Electron Microscope at 100 keV.
548
549 **Cryo-EM grid preparation and data collection of CRY:TIM complex**
550 Four µL of 0.5 mg/ml CRY:TIM solution was applied to glow-discharged grids (300 mesh
551 Quantifoil Au, R1.2/1.3) that were purchased from Electron Microscopy Sciences. After 30
552 seconds incubation, the excess solution was blotted for 4 sec with filter paper by a Vitrobot Mark
553 IV (Thermo Fischer Scientific). Grids were subsequently vitrified in liquid ethane and stored in
554 liquid nitrogen. Cryo-EM images of CRY:TIM complex were collected on a Talos Arctica (Thermo
555 Fischer Scientific) operated at 200 keV at a nominal magnification of 79,000x with Gatan GIF
556 Quantum LS Imaging energy filter, using a Gatan K3 direct electron camera in counting mode,
557 corresponding to a pixel size of 0.516 Å. A total of 1636 images stacks were obtained with a
558 defocus rage of -0.8 to -2.0 µm by EPU (Thermo Fischer Scientific). Each stack movie was
559 recorded for a total dose of 53 e-/Å2.
560
561 **Cryo-EM data processing of the CRY:TIM complex**
562 Dose fractionated image stacks were subjected to motioncor2[53] wrapped in Relion 3.1.3 [54]
563 followed by patch CTF estimation in CryoSparc v3.2.0[55]. The micrographs whose CTF estimation
564 is greater than 4 Å were chose for later processing, which yielded 1473 micrographs. Blob picker

565 in CryoSparc was used on the three hundred randomly selected micrographs, which was followed
566 by 2D classification and generation of ~23k particles for the first-round Topaz train[56]. Then the
567 trained model was applied to all 1473 micrographs and ~48k particles were extracted and selected
568 by 2D classification for the second-round of Topaz train particle identification. After two rounds of
569 Topaz train and extraction, in totality ~2M particles were picked. Following 2D classification non-
570 relevant particles were removed and only the best classes were kept (~350k particles). The
571 particle stack was subjected to Bayesian polishing in RELION 3.1.3 and imported back to
572 CryoSparc for the further Ab Initio reconstruction and Heterogenous refinement with 3 classes.
573 The second and third classes were selected, and multiple rounds of Homogenous and Non-
574 uniform Refinement were performed to yield a global 3.48 Å (~98k particles) and a global 3.3 Å
575 (~160k particles) map using "gold standard" FSC at 0.143 cut-off, respectively. The 3.3 Å map is
576 subjected to the model building. C1 symmetry was used throughout data processing. The
577 workflow is provided in Extended Figure 1.
578
579 **Model building and refinement of the CRY:TIM complex**
580 The initial CRY model is adapted from the PDB entry 4GU5, and the initial TIM model was fetched
581 from Alphafold Protein Structure Database entry P49021[57]. Both models were manually docked
582 into the map by UCSF ChimeraX[58]. The model was subjected to ISOLDE[59] to fit the loops which
583 undergo conformational changes into the map density. Intrinsically disordered loops of TIM which
584 were not visualized in the map were not included in the model. The CRY:TIM model was subjected
585 to multiple rounds of automatic refinement using Phenix real space refinement, and manually
586 building using Coot[60-62]. Validation was performed by MolProbity[63]. The final refinement statistics
587 is provided in Table S1.
588
589 The unassigned polypeptide in the TIM grove was built in both directions and the sequence
590 register slid along the backbone for a 150 residue stretch in the 250-400 range and each register
591 real-spaced refined against the electron density and Q-score [64] calculated. Given the helical
592 nature of the density at one end of the groove, directionality of the sequence was best fit with the
593 polypeptide having its N-terminal end closest to CRY and the C-terminal end running toward the
594 Lys313/328 crosslinking partners at the base of the groove. Side chain density in the helical region
595 showed a variable size pattern that was inconsistent with the repetitive patterns of much of the
596 disordered region beyond residue 350. C-terminal to the groove peptide Lys313 and Lys328 are
597 unresolved, but should be closely positioned to their crosslinking partners. To assign sequence
598 to the disconnected TIM helix binding the PHR C-terminus secondary structure predictions on the

regions of TIM not resolved in the ordered core were performed by RAPTORX[65]. All predicted helical sequences were fit into the density and refined in real-space with a range of sequence registers. As an additional check Alphafold2.0[57] was used to predict interactions between CRY and the disordered region of TIM, with the highest scoring predictions also tested for agreement with the electron density map. Although Alphafold did predict interactions of TIM in the region of the peripheral helix, none of the predictions aligned well with the observed density. The disconnected helix displays strong side-chain density, which sets its directionality and ruled out many sequence placements. Given the resolution limitations of the cryo-EM maps, we consider the sequence assignments of both of these helical regions tentative.

Methods References

51 Lin, C., Schneps, C. M., Chandrasekaran, S., Ganguly, A. & Crane, B. R. Mechanistic insight into light-dependent recognition of Timeless by Drosophila Cryptochrome. *Structure* doi:10.1016/j.str.2022.03.010 (2022).

52 Muok, A. R. *et al.* Engineered chemotaxis core signaling units indicate a constrained kinase-off state. *Science Signaling* **13** (2020).

53 Zheng, S. Q. *et al.* MotionCor2: anisotropic correction of beam-induced motion for improved cryo-electron microscopy. *Nat Methods* **14**, 331-332 (2017).

54 Scheres, S. H. RELION: implementation of a Bayesian approach to cryo-EM structure determination. *J Struct Biol* **180**, 519-530 (2012).

55 Punjani, A., Rubinstein, J. L., Fleet, D. J. & Brubaker, M. A. cryoSPARC: algorithms for rapid unsupervised cryo-EM structure determination. *Nat Methods* **14**, 290-296 (2017).

56 Bepler, T. *et al.* Positive-unlabeled convolutional neural networks for particle picking in cryo-electron micrographs. *Nat Methods* **16**, 1153-1160 (2019).

57 Jumper, J. *et al.* Highly accurate protein structure prediction with AlphaFold. *Nature* **596**, 583-589 (2021).

58 Pettersen, E. F. *et al.* UCSF ChimeraX: Structure visualization for researchers, educators, and developers. *Protein Sci* **30**, 70-82 (2021).

59 Croll, T. I. ISOLDE: a physically realistic environment for model building into low-resolution electron-density maps. *Acta Crystallogr D Struct Biol* **74**, 519-530 (2018).

60 Morin, A. *et al.* Collaboration gets the most out of software. *Elife* **2**, e01456 (2013).

61 Emsley, P., Lohkamp, B., Scott, W. G. & Cowtan, K. Features and development of Coot. *Acta Crystallogr D Biol Crystallogr* **66**, 486-501 (2010).

633 62 Liebschner, D. *et al.* Macromolecular structure determination using X-rays, neutrons and
634 electrons: recent developments in Phenix. *Acta Crystallogr D Struct Biol* **75**, 861-877
635 (2019).

636 63 Chen, V. B. *et al.* MolProbity: all-atom structure validation for macromolecular
637 crystallography. *Acta Crystallogr D Biol Crystallogr* **66**, 12-21 (2010).

638 64 Pintilie, G. *et al.* Measurement of atom resolvability in cryo-EM maps with Q-scores. *Nat*
639 *Methods* **17**, 328-334 (2020).

640 65 Kallberg, M. *et al.* Template-based protein structure modeling using the RaptorX web
641 server. *Nature Protocols* **7**, 1511-1522 (2012).
642

643 **Data availability** The cryo-EM density maps and the atomic model for TIM:CRY have been
644 deposited in the EM Data Bank (EMDB: EMD-27335) and Protein Data Bank (PDB: 8DD7),
645 respectively. The mass spectrometry proteomics data have been deposited to the
646 ProteomeXchange Consortium via the PRIDE partner repository with the dataset identifier
647 PXD034054.
648

649 **Acknowledgements** We thank the Proteomics and Metabolomics Facility of Cornell University
650 for providing the mass spectrometry data; Katherine Spoth and Mariena Silvestray-Ramos for
651 help with EM instrumentation; Yitong Li for suggesting use of the ALFA Tag and experimental
652 assistance, Greg Merz, Thuy-Tien Nguyen, and Cody Aplin for general aid; and Richard Cerione
653 and Michael Young for helpful feedback. Figures 1A, inlet in 2B, 4D, and S1 were created with
654 BioRender.com. This work was supported by NIH grants R35GM122535 to BRC and 1S10
655 OD017992-01 for the Orbitrap Fusion mass spectrometer. This work made use of the Cornell
656 Center for Materials Research Shared Facilities which are supported through the NSF (DMR-
657 1719875).
658

659 **Author contributions** C.L., S.F., C.C.D, and B.R.C. designed research; C.L., S.F., C.C.D, and
660 B.R.C. conducted research; C.L., S.F., C.C.D, and B.R.C. analyzed data; C.L., S.F., C.C.D, and
661 B.R.C. wrote the manuscript.
662

663 **Competing interests** The authors declare that they have no competing interests.

664 **Extended Data Figure 1. CRY:TIM purification and cryo-EM workflow.** Purification of
665 CRY:TIM complexes for cryo-EM. (a) SDS-PAGE gel showing complex after elution from the
666 ALFA resin, followed by crosslinking, followed by SEC. (b) SEC trace of purified complex, peak I:
667 aggregates, peak II: CRY-TIM complex, and peak III: excessive ALFA peptide. (c) Processing
668 workflow for CRY:TIM collected on a Talos Arctica (Thermo Fischer Scientific) operated at 200
669 keV using a Gatan K3 direct electron camera. The red box indicates the final reconstruction in
670 this study. Data processing was carried out in CryoSparc and RELION. Motion Correlation was
671 performed by RELION (MotionCor2); with Contrast Transfer Function (CTF) applied in CryoSparc.
672 Topaz was used for particle classification. Overall resolution determination in CryoSparc by Gold
673 Standard Fourier Shell Correlation (GSFSC) is shown at the mid-bottom left. Corrected values
674 give 3.30 Å overall resolution. Local resolution exceeds 2.5 Å, as shown on the bottom right.
675 Particle orientational sampling is reasonably uniform as shown at the bottom left. Number of
676 particles (images) holding a given azimuthal and elevation angle are indicated in the 2-
677 dimensional histogram.

678 **Extended Data Figure 2. TIM domain construction and secondary structure assignments**.
679 Domain construction and secondary structure assignments of TIM.
680

681 **Extended Data Figure 3. CRY domain construction and secondary structure assignments.**
682 Domain construction and secondary structure assignments of CRY.
683

684 **Extended Data Figure 4. Key interactions at the CRY:TIM interface.** (a) Interactions between
685 the bottom half of TIM ARM_1-α1 with CRY. ARM1- α1 binds across CRY α14 and α17. The
686 guanidinium of CRY R446 (on α17) forms π-cation interaction with TIM Y11. TIM Y11 participates
687 in hydrophobic contacts with CRY P257, L443 and L447. On TIM α1, TIM P8 stacks against CRY
688 α12 and TIM S15 hydrogen bonds to the backbone carbonyl of CRY A442. (b) In the β-hairpin
689 connecting ARM_1- α1 to ARM_1- α2 E21 salt-bridges to R474 and C19 interacts with K445. (c)
690 Interactions of the CRY protrusion motif. TIM R109, F113, and H110 interact with the protrusion
691 motif of CRY. TIM ARM_2-α3 H110 stacks with CRY H307. Four Met residues (M179, M181 M182,
692 M185) in the ARM_3-α2-α3 loop provide side-chain interactions with the tip of the CRY protrusion
693 motif. The CRY α10 helix lengthens to residue A295 compared to the dark state and the following
694 300-306 residues interact directly with ARM_2-α3. (d) Interactions of the CRY C-terminal lid and
695 α20 helix. The restructured C-terminal lid interacts with residues on TIM ARM_1- α2. For examples,
696 L34 make a hydrophobic contact with I436 and E37 hydrogen bonds to the backbone of S434. At

697 the end of ARM_1- α2, Asn30 contacts the N-terminal end of CRY α20. A DSSO crosslink observed
698 between Lys510 on CRY a20 and Lys41 on ARM1-α3 is fully consistent with the observed
699 interface.
700
701 **Extended Data Figure 5. Changes in flavin binding pocket for CRY dark and bound states.**
702 Comparison of the flavin pocket in CRY:TIM compared to in dark-state CRY (PDB 4GU5). (a) In
703 CRY:TIM, Y250 and L251 interact with the FAD pocket and make space for the top of TIM ARM_1-
704 α3 to insert F58 behind the new conformation of the phosphate-binding loop. (b) The FAD adenine
705 ring of CRY:TIM slides 1.5 Å relative to the unbound structure. CRY F318 shifts away from its
706 original position and harbors helix α11 to compensate for the FAD adenine ring adjustment,
707 following the protrusion motif. (c) G311 swivels away from the inserted TIM L4. New diphosphate
708 conformations cause rearrangement of the CRY 262-to-264 loop.
709
710 **Extended Data Figure 6. Exit channel at the CRY:TIM interface and CRY secondary pocket.**
711 (a) Putative exit channel for the additional 23 N-terminal residues of L-TIM. The first residue of
712 TIM (M1) is colored as red. A solvent accessible channel at the interface between the two proteins
713 is marked as the green arrow. (b) Electron density for the secondary binding pocket of CRY where
714 antenna cofactors bind in photolyases and mCRY interact with other Clock proteins (**red** box)
715 CRY (**yellow**), TIM (**periwinkle blue**), TIM 1163-1174 (**blue**), TIM groove (**navy blue**). Although
716 the pocket is well formed, there is no obvious density for additional moieties.
717
718 **Extended Data Figure 7. TIM peripheral helix and groove peptide fitting to the electron**
719 **density map and associated Q-scores.** (a) Real-space electron density fitting metrics for the
720 top scoring sequence assignments for the TIM peripheral helix. Real space density agreements
721 were calculated in Q-scores and are shown above for sidechains and below for mainchains. (b)
722 Real-space electron density fitting metrics for the top scoring sequence assignments for the TIM
723 groove-binding polypeptide. Real space density agreements were calculated in Q-scores and are
724 shown above for sidechains and below for mainchains. The TIM groove binding polypetide was
725 tested in both directions.
726
727 **Extended Data Figure 8. Relative binding affinities between fragments of TIM and CRY**
728 **H377L by the SWFTI assay.** (a) The CRY H377L variant enhances binding affinity for TIM by
729 stabilizing the TIM-binding conformation of CRY and thereby increases TIM expression levels and

730 overall facilitates detection of weaker binding variants. sample size = 3. One-way anova was used
731 to analyze p value. * represents $p<0.05$, ** $p<0.01$ (b) Pull down results of CRY-H377L with TIM-
732 1133-1398. CRY-H377L interacts with the C-terminal regions of TIM. (c) Quantification of the
733 binding strength between CRY-H377L and TIM (1133-1398) compared to the negative control
734 (CRY-H377L only with the same amount of resin). The binding strength is defined as the amount
735 of CRY on the resin divided by the amount of CRY in the lysate sample. The negative control is
736 normalized to 1. Sample size = 3. Two-tailed t-test yields a p value < 0.0001 (****). Binding
737 affinities could not be derived from this experiment owing to the challenge of producing excessive
738 CRY relative to TIM 1133-1398.
739
740 **Extended Data Figure 9. Comparisons of structural features in the CRY:TIM complex to**
741 **those of CRY and TIM homologues.** (a) Structural comparison of CRY:TIM with mammalian
742 CRY bound with mammalian PER. TIM 1163-1174 (**blue**) follows the backbone trace of mPER
743 (CRYΔ (**yellow**), TIM BD2 1163-1174 (**blue**)). 4CT0: Crystal Structure of Mouse Cryptochrome1
744 in Complex with Period2 (**magenta**). 4U8H: Crystal Structure of Mammalian Period-
745 Cryptochrome Complex (**green**). 6OF7: Crystal structure of the CRY1-PER2 complex (**orange**
746 **red**). (b) Structural comparison of CRY:TIM (CRY (**yellow**), TIM (**periwinkle blue**), TIM 1163-
747 1174 (**blue**), TIM groove peptide (**navy blue**)) with the crystal structure of the N-terminal domain
748 of human Timeless (PDB ID: 5MQI, **salmon**). Note that mammalian TIM does not contain the N-
749 terminal residues that bind into the CRY flavin pocket. (c) Structural superposition of TIM PAB
750 (PARP-1 binding) domain with the structure of human TIM PAB bound to the PARP-1 catalytic
751 domain. Red box highlights the TIM α-helix occupying the same space required for PARP-1
752 binding. TIM (this study, **periwinkle blue**), 4XHU (PAB:**sky blue**, PARP-1:**charcoal**). (d)
753 Superposition of TIM and Tof1 within the replisome.
754
755 **Extended Data Figure 10. Interactions between TIM and its homologs with extended**
756 **polypeptides in their respective ARM grooves in relation to crosslinking map of CRY:TIM.**
757 (a) Sequence alignment of top TIM structural homologs as calculated by the DALI server[50]. Boxes
758 outline the conserved R-XXX-N and RN residues within the ARM motifs that interact with the
759 extended polypeptide chains of binding partners. Protein Data Bank (PDB) codes are shown on
760 the left. (b) The extended peptide bound in the TIM groove resembles interactions found in other
761 ARM-repeat proteins such as Importin-α1, β-catenin, and yeast TIM proteins. ARM-repeat
762 proteins were structurally superimposed by their ARM-repeat cores to show the alignment of the
763 extended peptides that bind in the crescent groove common to the family. For clarity only the

764 groove peptides are displaced. Extended polypeptides found in yeast TOF1 (6SKL) and β-catenin
765 (3IFQ) and TIM travel on the same lateral axis anti-parallel to the other importin- $\boldsymbol{\alpha}$, β-catenin, and
766 TIM protein homologues. The PDB labels indicate the N-terminus of the loop. 6SKL: Cryo-EM
767 structure of the CMG Fork Protection Complex at a replication fork - Conformation 1 (lavender),
768 3IFQ: Interaction of plakoglobin and β-catenin with desmosomal cadherins (**gold**), 1JDH: Crystal
769 structure of β-catenin and htcf-4 (**purple**), 3L3Q: Mouse importin $\boldsymbol{\alpha}$-pepTM NLS peptide complex
770 (gray), 3KND: TPX2:importin-αlpha complex (**magenta**), 1IQ1: Crystal structure of the importin-
771 $\boldsymbol{\alpha}$(44-54)-importin-$\boldsymbol{\alpha}$(70-529) complex (**salmon**), 3UKX: Mouse importin-$\boldsymbol{\alpha}$:Bimax2 peptide
772 complex (**sky blue**). (c) Map of DSSO lysine residue crosslinking defined by mass spectroscopy
773 for the CRY:TIM complex. For the LysC+trypsin digested sample, although +2-charged peptides
774 were excluded in the analysis, 59.79% sequence coverage for CRY and 49.81% for TIM were
775 obtained. For the LysC+trypsin+GluC digested sample, 25.07% sequence coverage was obtained
776 for CRY and 25.53% sequence coverage was obtained for TIM. Summary of the cross-links are
777 given in the attached excel files and the raw data has been submitted to the PRIDE database.

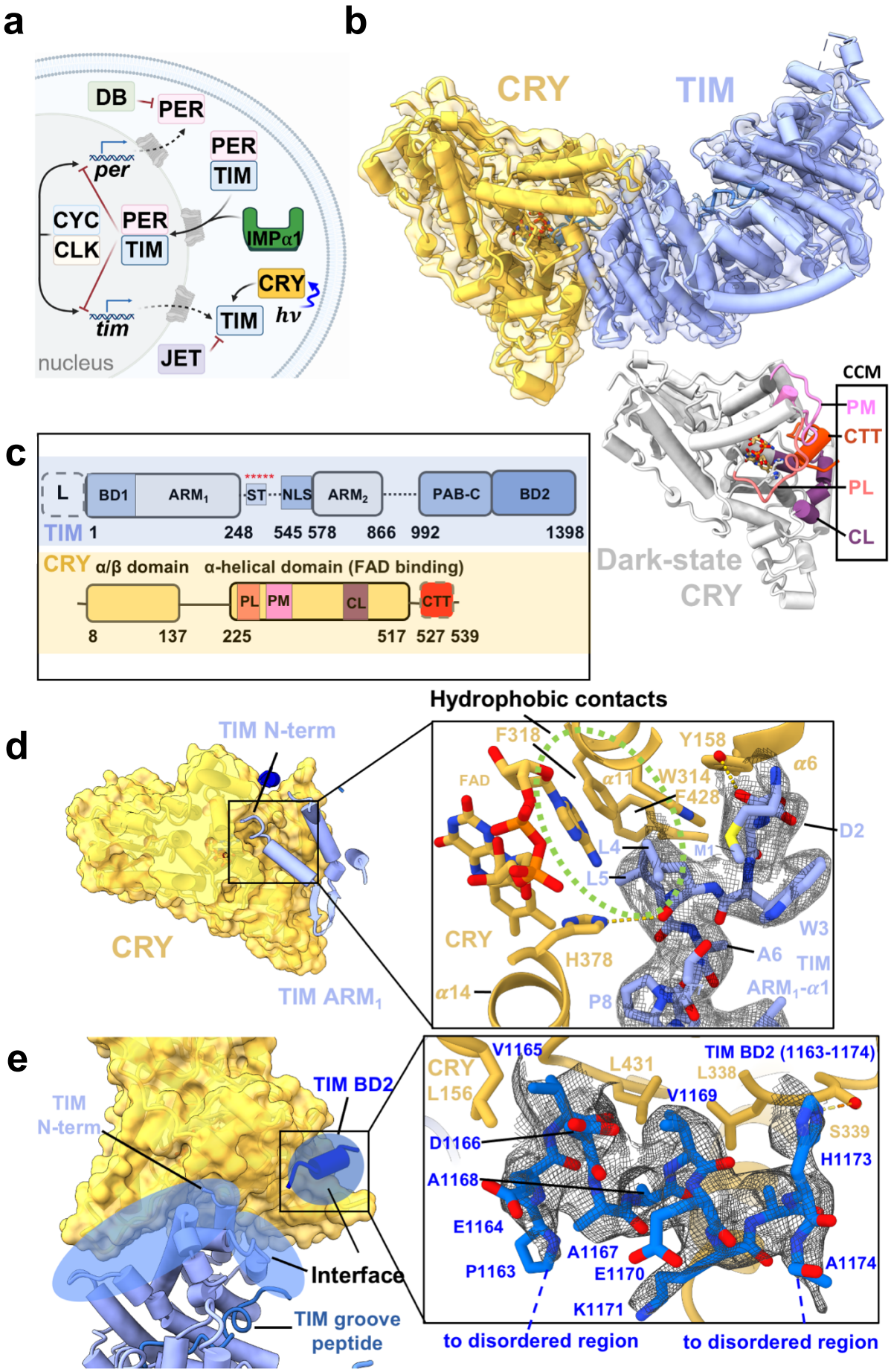
a
DB
PER
PER
TIM
per
CYC
CLK
PER
TIM
IMPα1
CRY
hν
TIM
tim
JET
nucleus
b
CRY
TIM
CCM
PM
CTT
PL
CL
Dark-state
CRY
c
L
BD1
ARM1
ST
NLS
ARM2
PAB-C
BD2
TIM 1
248
545 578
866
992
1398
CRY α/β domain
α-helical domain (FAD binding)
PL
PM
CL
CTT
8
137
225
517
527 539
d
TIM N-term
CRY
TIM ARM1
Hydrophobic contacts
F318
Y158
α6
FAD
α11
W314
F428
D2
L4
M1
L5
W3
CRY
H378
A6
TIM
ARM1-α1
α14
P8
e
TIM
N-term
TIM BD2
Interface
TIM groove
peptide
CRY
V1165
L431
TIM BD2 (1163-1174)
L156
L338
V1169
S339
D1166
H1173
A1168
E1164
A1167
P1163
E1170
A1174
K1171
to disordered region
to disordered region

Figure 1. Cryo-EM structure of the CRY:TIM complex. (**a**) Drosophila Cryptochrome (CRY) entrains the circadian clock by initiating degradation of Timeless (TIM) in light. Jetlag (JET), Period (PER), Doubletime (DB), Cycle (CYC), Clock (CLK) and Importin-α1 (IMPα1) compose the core circadian oscillator. (**b**) CRY:TIM docked into the electron density map. Dark-state CRY shown at the bottom (grey, PDB ID: 4GU5). (**c**) Domain arrangements and key regions of CRY and TIM. Features of TIM: CRY-binding domains (CRY-BD1, 1-234, CRY-BD2, 1133-1398), serine/threonine-rich region (ST, 270-290) with key phosphorylation sites starred (S274, T278, T282, S286 and S290), ARM1 (1-248), ARM2 (578-866), nuclear localization sequence (NLS, 545-578), Parp-1 binding domain (PAB, 986-1142; TIM-C, 1051-1096), 23 residue L-TIM extension (L, (23aa)), disordered regions are dashed. Features of CRY: Phosphate binding loop (PL, 249-263), Protrusion motif (PM, 288-306), C-terminal lid (CL, 420-446), C-terminal tail (CTT, 519-542, absent in CRYΔ). (**d**) N-terminus of TIM inserts into the primary flavin binding pocket. 2.4 Å resolution local electron density is shown with notable hydrogen bonds (yellow dashes) and hydrophobic contacts (green circle). (**e**) Interface between CRY and TIM (blue shaded area), TIM groove peptide (in navy blue) and peripheral helix (fitted with 1163-1174 putatively, blue). Inset shows the interactions between TIM 1163-1174 and CRY superimposed with electron density.

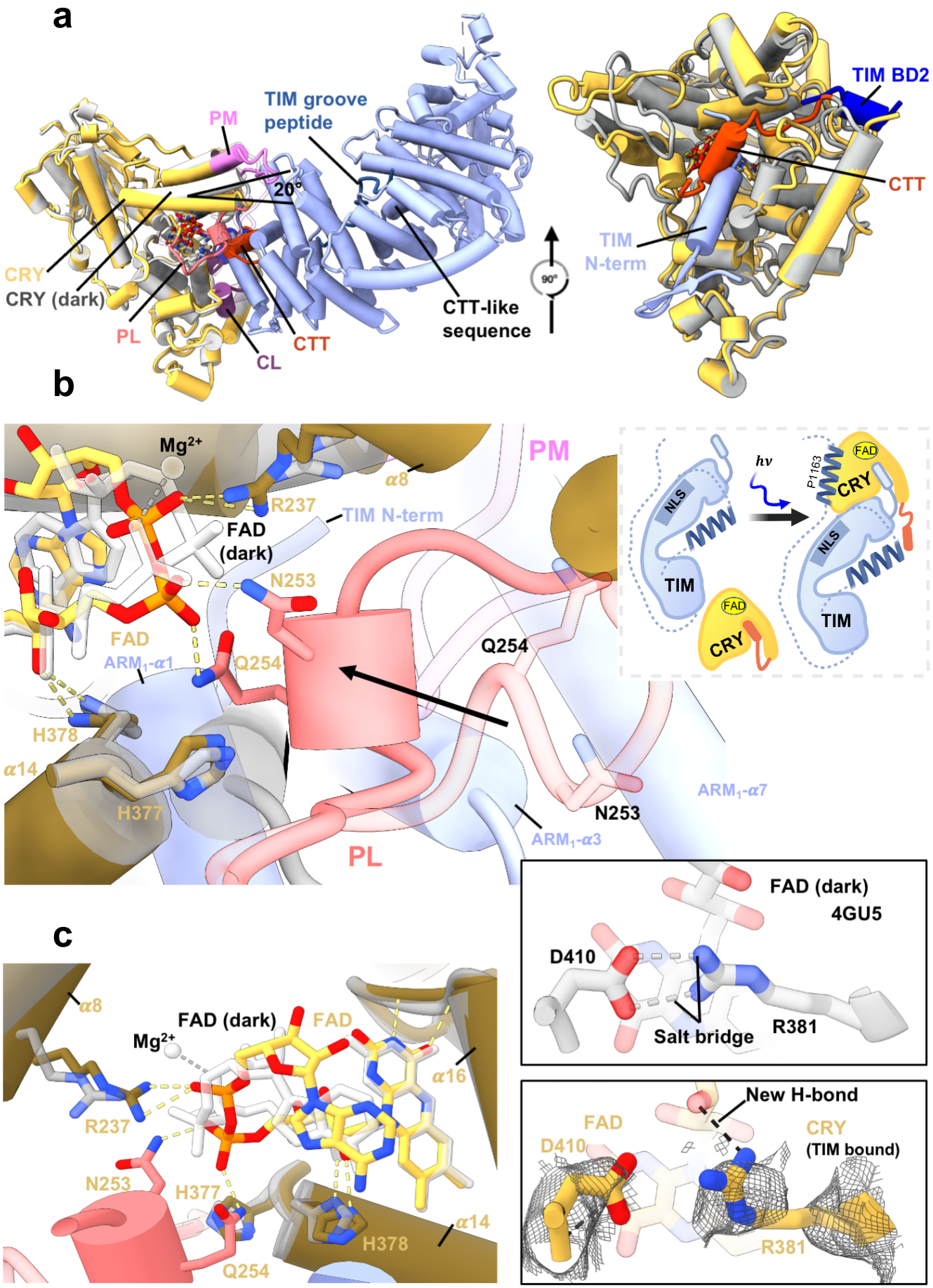
a
PM
TIM groove peptide
20°
CRY
CRY (dark)
PL
CL
CTT
CTT-like sequence
90°
TIM BD2
CTT
TIM N-term
b
Mg2+
PM
α8
R237
TIM N-term
FAD (dark)
N253
FAD
ARM1-α1
Q254
Q254
H378
α14
H377
N253
ARM1-α7
ARM1-α3
PL
hν
P1163
FAD
CRY
NLS
TIM
FAD
CRY
NLS
TIM
c
α8
FAD (dark)
FAD
Mg2+
α16
R237
N253
H377
α14
H378
Q254
FAD (dark)
4GU5
D410
Salt bridge
R381
New H-bond
FAD
D410
CRY
(TIM bound)
R381

Figure 2. Conformational changes of FAD to the CRY C-terminal coupled motif upon binding TIM. (**a**) CRY:TIM (CRY, yellow; TIM, blue) in superposition with dark-state CRY. The N-terminus of TIM replaces the CRY CTT (red), as depicted in the schematic below. Structural elements designated as in **Figure 1**. (**b**) The phosphate binding loop (dark pink) collapses into the flavin pocket and N253 and E254 hydrogen bond (yellow dashes) with the FAD diphosphate conformation (red, orange) that differs substantially from that of the dark state (white bonds). (**c**) R237 replaces the Mg^{2+} counter ion and H377 anchors the new position of the loop. The D410-R381 salt bridge (top) appears to break in response to the new conformation of the ribose backbone (bottom). Reduced side-chain density of R381 suggests increased flexibility in the TIM complex.

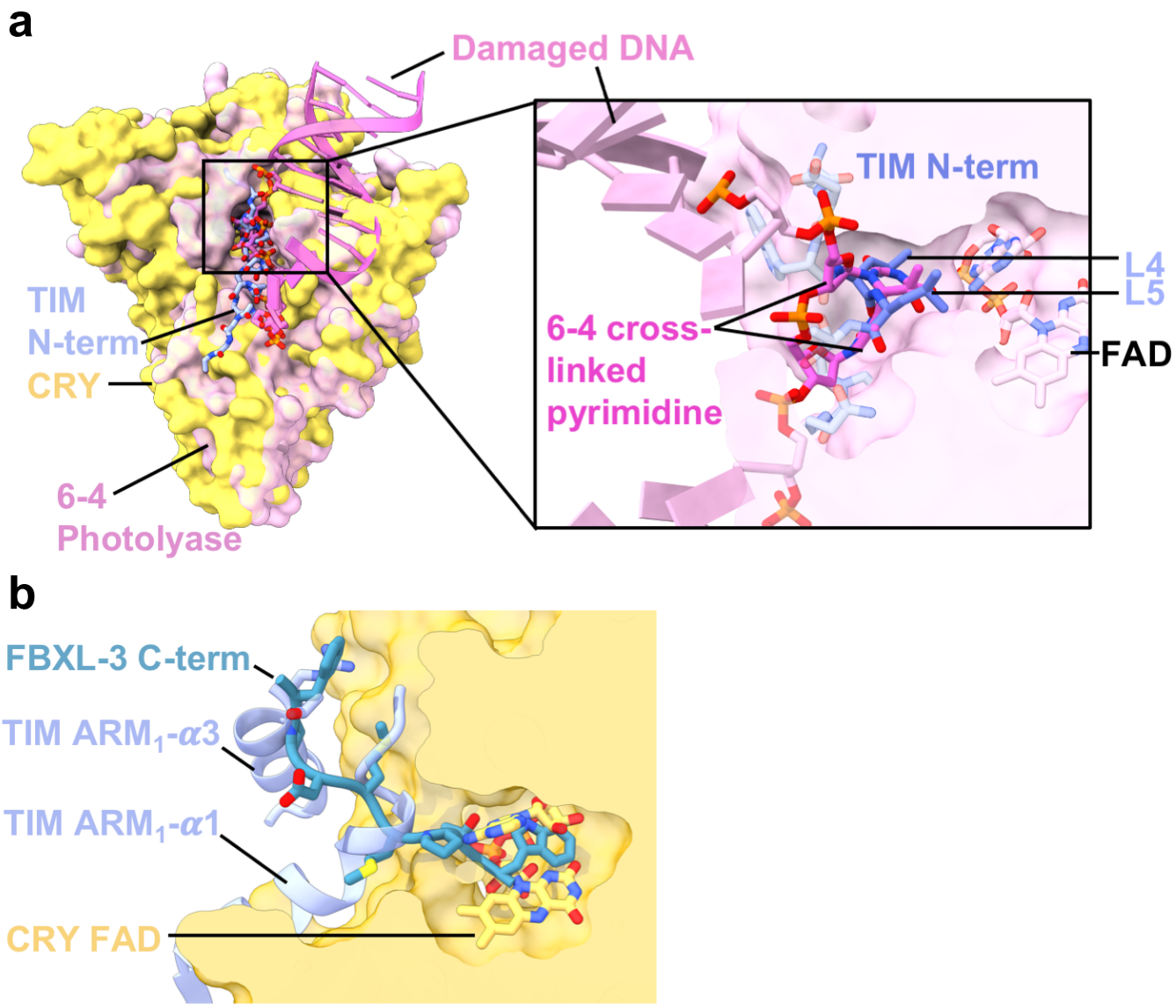
a
Damaged DNA
TIM N-term
L4
L5
FAD
6-4 cross-linked pyrimidine
TIM N-term
CRY
6-4 Photolyase
b
FBXL-3 C-term
TIM ARM$_1$-α3
TIM ARM$_1$-α1
CRY FAD

Figure 3. Conservation of recognition modes by CRY family members. (**a**) The interaction of CRY with TIM corresponds closely to how 6-4 photolyase recognizes the 6-4 pyrimidine lesion in damaged DNA (PDB ID:3CVU). TIM Leu4 and Leu5 superimpose on the crosslinked bases and the TIM ARM1- α1 polypeptide closely follows the path of 5'-to-3' strand-separated DNA. (**b**) The TIM and FAD contacts of CRY mimic the interaction of apo-mCRY with the C-terminus of the FBXL3 E3 ligase (PDB ID: 4I6J).

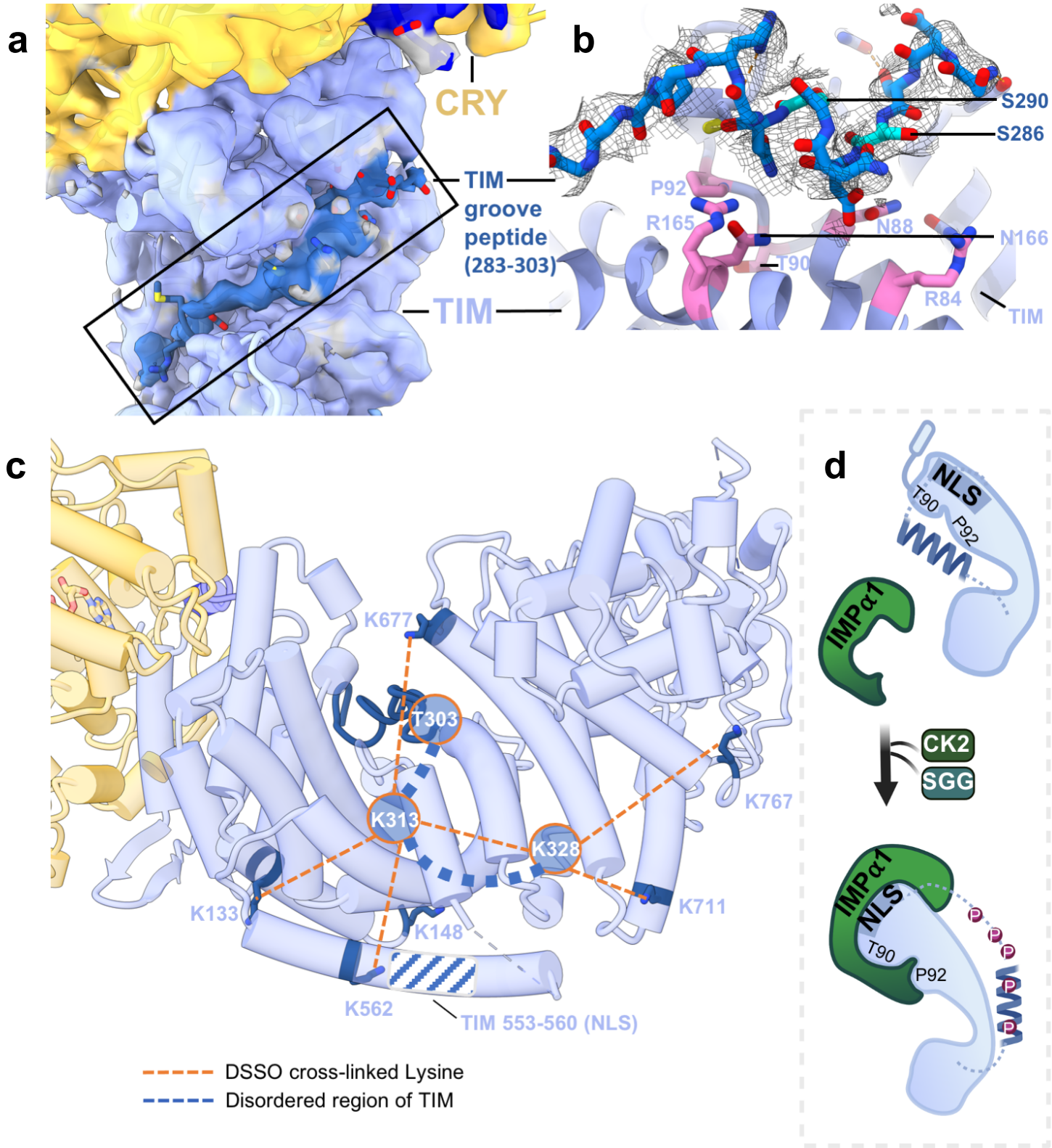
a
CRY
TIM
groove
peptide
(283-303)
TIM
b
S290
S286
P92
R165
N88
N166
T90
R84
TIM
c
K677
T303
K313
K328
K767
K133
K148
K711
K562
TIM 553-560 (NLS)
DSSO cross-linked Lysine
Disordered region of TIM
d
NLS
T90
P92
IMPα1
CK2
SGG
IMPα1
NLS
T90
P92
P
P
P
P
P

Figure 4. A structural basis for regulation of TIM nuclear entry. (**a**) Electron density (dark blue) for an extended polypeptide resides within a groove wherein members of the β-catenin and α-importin proteins bind their target sequences. (**b**) The TIM groove peptide density shown with the sequence assignment S283-T303. The peptide interacts with β-catenin-conserved Asn and Arg residues and buries residues important for importin-α1 binding (T90 and P92). (**c**) DSSO-mediated lysine crosslinking patterns of disordered residues K313 and K238 shown on the TIM structure. K313 and K328 produce a pattern of crosslinking that localizes them to a position consistent with placement of the S283-T303 groove peptide. The TIM NLS lies in a helix adjacent to the groove but does not occlude T90 and P92. (**d**) Schematic of proposed nuclear entry mechanism of TIM. Phosphorylation of the TIM-ST region by SGG and CK2 releases the ST region from TIM groove to expose TIM T90 and P92. Importin-α1 recognizes TIM by binding adjacent to Thr90 and Pro92, while also binding the TIM NLS within a structurally analogous ARM groove of its own.

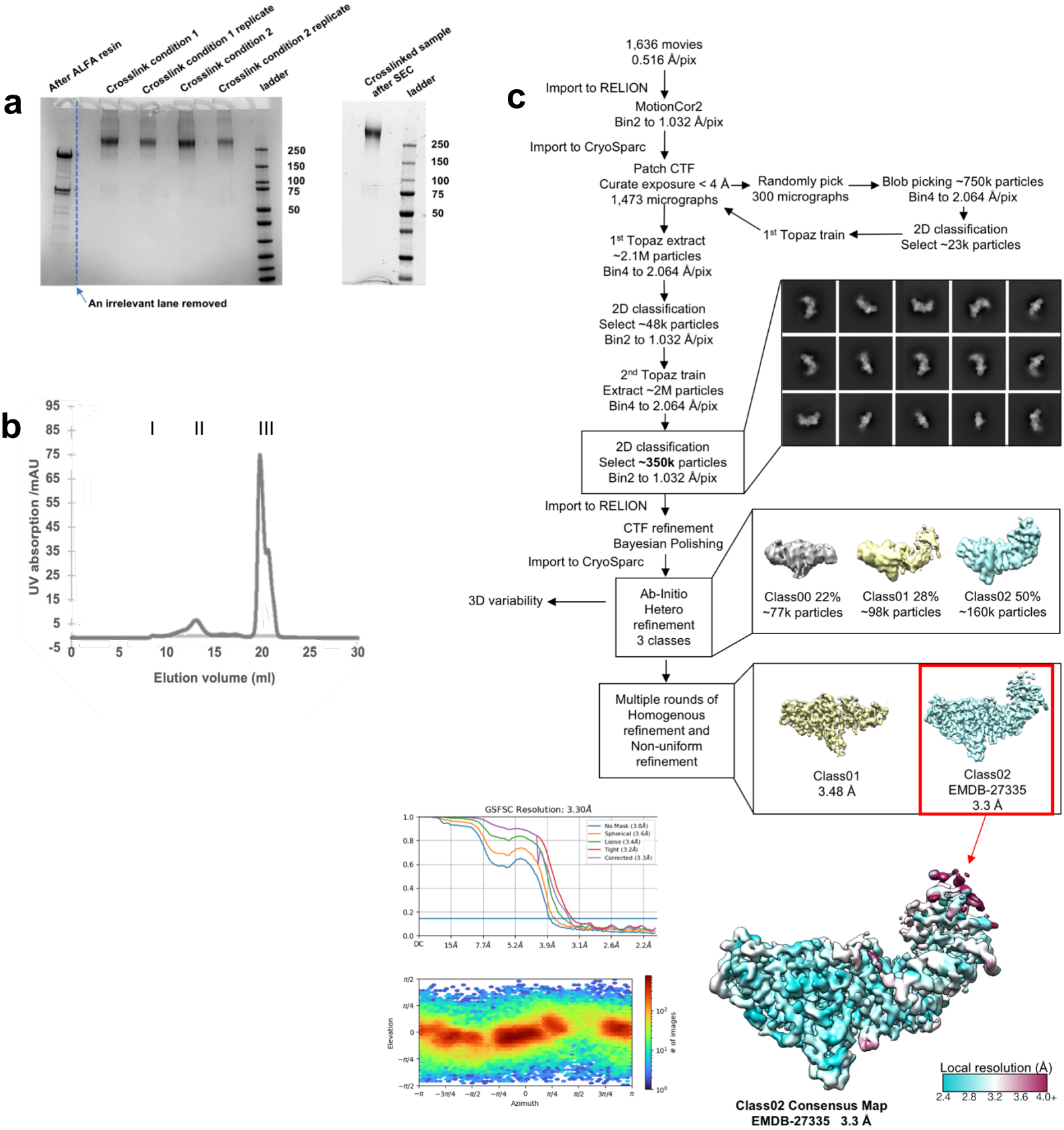

Extended Data Fig. 1

Extended Data Figure 1. CRY:TIM purification and cryo-EM workflow. Purification of CRY:TIM complexes for cryo-EM. (a) SDS-PAGE gel showing complex after elution from the ALFA resin, followed by crosslinking, followed by SEC. (b) SEC trace of purified complex, peak I: aggregates, peak II: CRY-TIM complex, and peak III: excessive ALFA peptide. (c) Processing workflow for CRY:TIM collected on a Talos Arctica (Thermo Fischer Scientific) operated at 200 keV using a Gatan K3 direct electron camera. The red box indicates the final reconstruction in this study. Data processing was carried out in CryoSparc and RELION. Motion Correlation was performed by RELION (MotionCor2); with Contrast Transfer Function (CTF) applied in CryoSparc. Topaz was used for particle classification. Overall resolution determination in CryoSparc by Gold Standard Fourier Shell Correlation (GSFSC) is shown at the mid-bottom left. Corrected values give 3.30 Å overall resolution. Local resolution exceeds 2.5 Å, as shown on the bottom right. Particle orientational sampling is reasonably uniform as shown at the bottom left. Number of particles (images) holding a given azimuthal and elevation angle are indicated in the 2-dimensional histogram.

TIM ARM$_1$:

α1: 1 - 17
α2: 31 - 44
α3: 51 - 59
α4: 61 - 72
α5: 76 - 89
α6: 92 - 102
α7: 106 -126
α8: 129 - 145
α9: 151 - 177
α10: 185 - 201
α11: 204 - 213
α12: 217 - 231
α13: 237 - 247

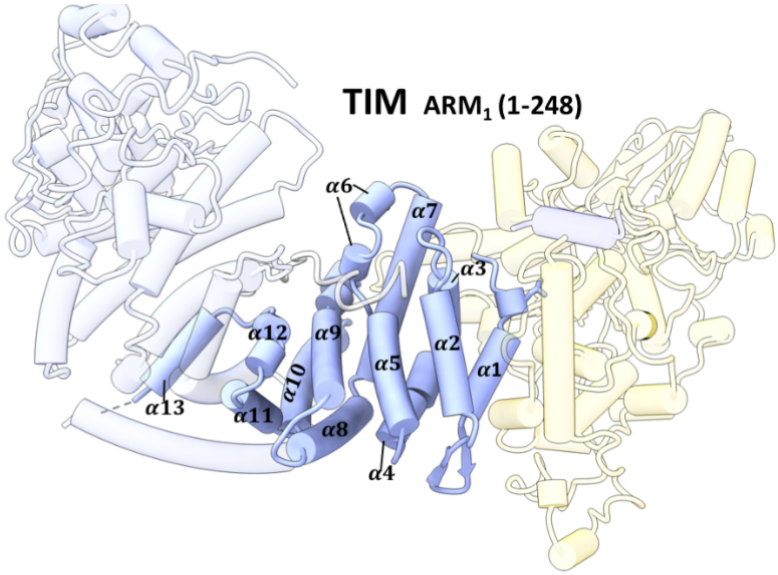

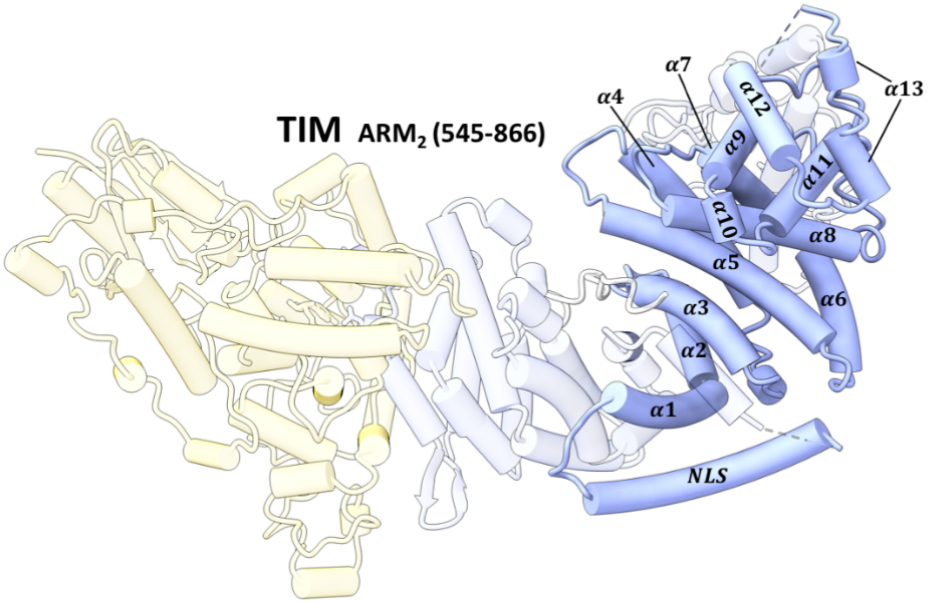

TIM ARM$_2$:

NLS: 546 - 570
α1: 578 - 595
α2: 597 - 608
α3: 618 - 634
α4: 648 - 668
α5: 677 - 702
α6: 709 - 722
α7: 726 - 736
α8: 745 - 765
α9: 787 - 797
α10: 799 - 802
α11: 807 - 818
α12: 830 - 842
α13: 848 - 862

TIM PAB-C:

α1: 991 - 1002
α2: 1006 - 1017
α3: 1020 - 1027
α4: 1040 - 1046
α5: 1059 - 1066
α6: 1068 - 1076
α7: 1103 -1107

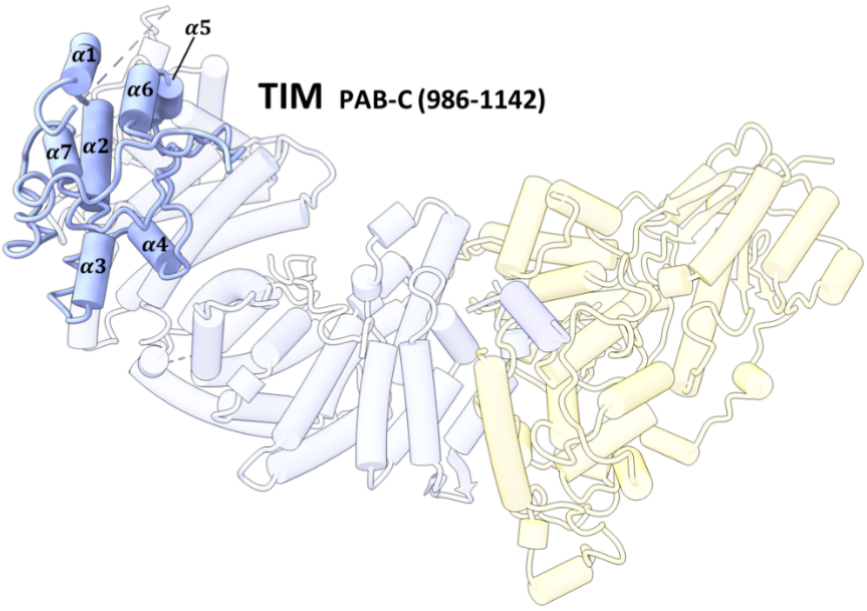

Extended Data Fig. 2

Extended Data Figure 2. TIM domain construction and secondary structure assignments. Domain construction and secondary structure assignment of TIM.

CRY N-terminal
α/β domain:
β1: 6 - 11
α1: 21 - 32
β2: 35 - 42
α2: 54 - 75
β3: 82 - 85
α3: 88 - 98
β4: 101 - 106
α4: 112 - 128
β5: 131 - 135

Linker region (not highlighted)
α5: 143 - 149
α6: 159 - 168
α7: 190 - 195

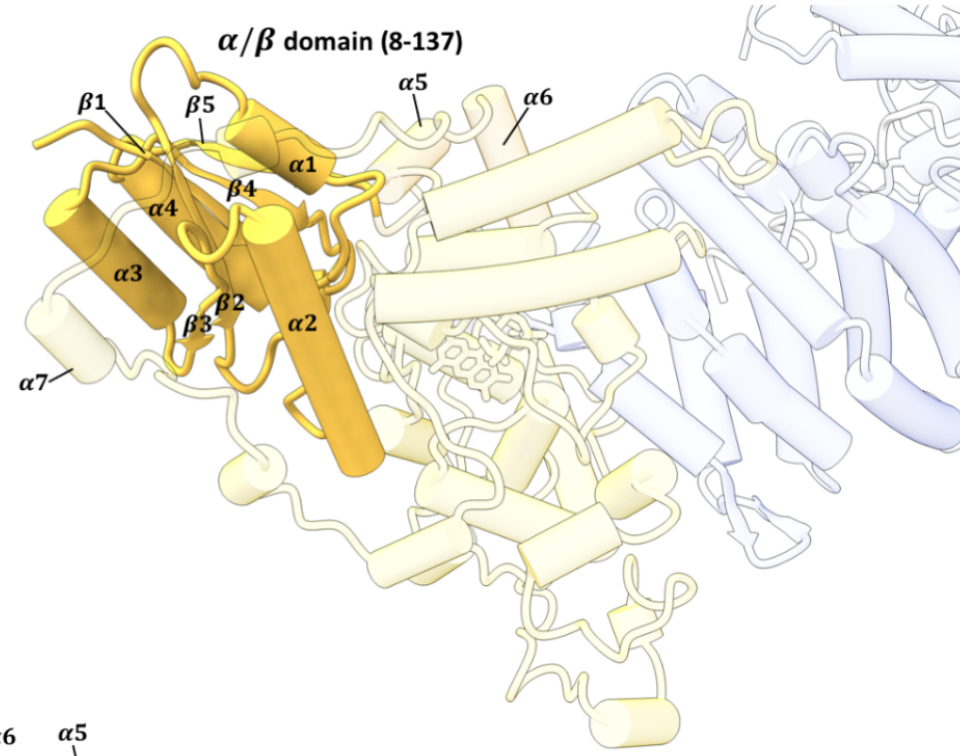

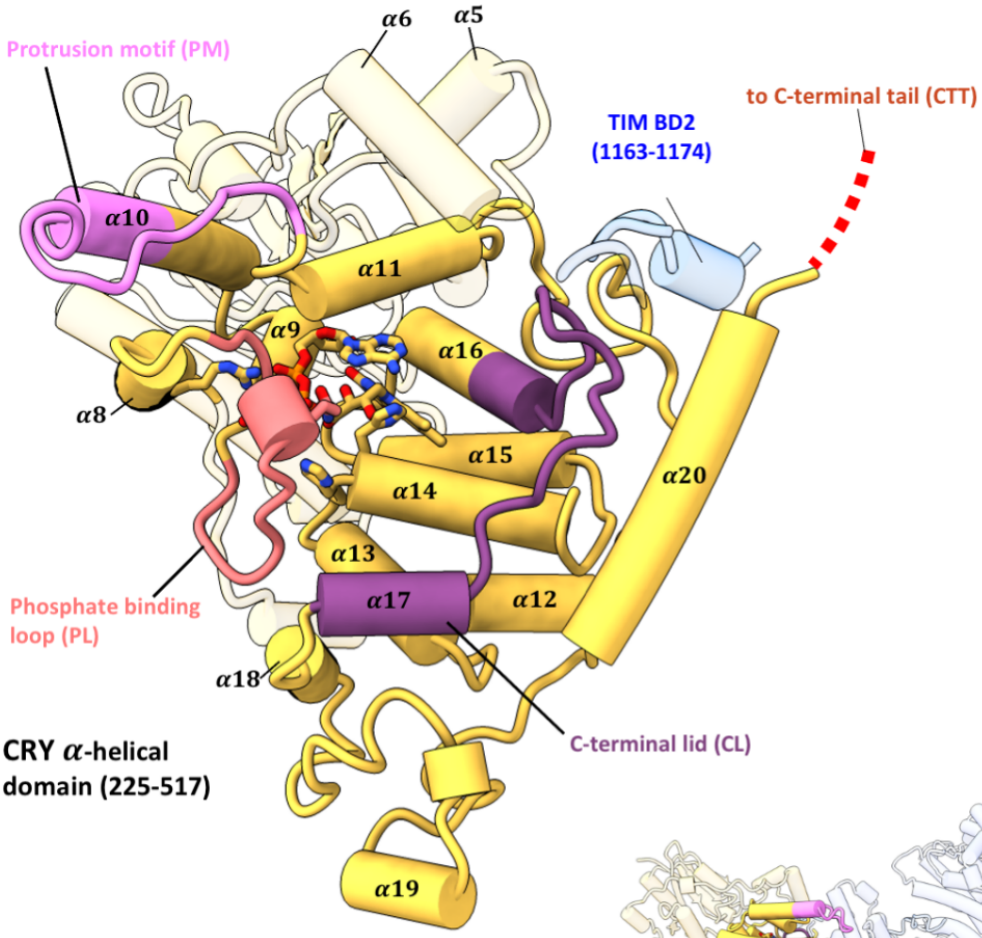

CRY α-helical domain (225-517)

CRY α-helical domain (FAD binding):
α8: 227 - 247
α9: 267 - 272
α10: 277 - 288
(277-293 in CRY:TIM complex)
α11: 310 - 321
α12: 347 - 355
α13: 361 - 372
α14: 378 - 388
α15: 397 - 406
α16: 413 - 424
α17: 440 - 447
α18: 452 - 457
α19: 477 - 482
α20: 498 - 515

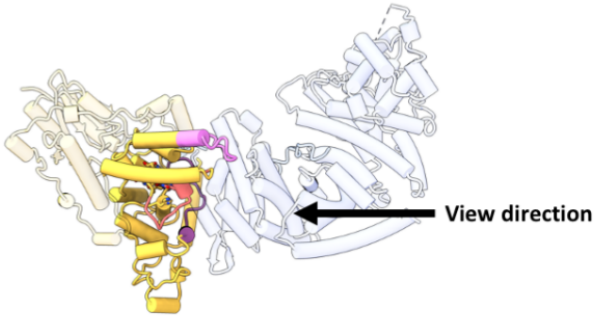

Extended Data Fig. 3

Extended Data Figure 3. CRY domain construction and secondary structure assignments. Domain construction and secondary structure assignment of CRY.

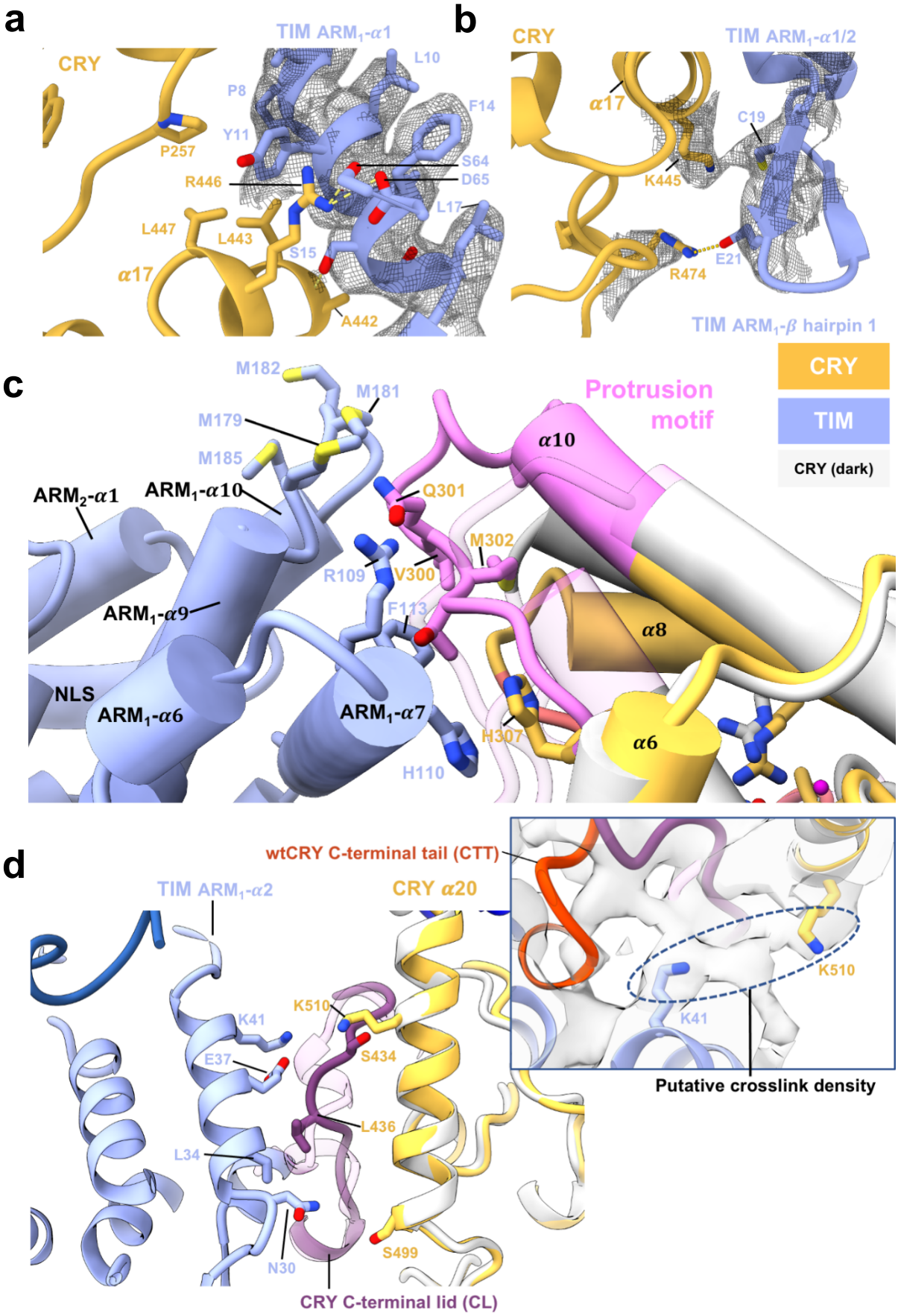

Extended Data Fig. 4

Extended Data Figure 4. Key interactions at the CRY:TIM interface. (a) Interactions between the bottom half of TIM ARM_1-α1 with CRY. ARM1- α1 binds across CRY α14 and α17. The guanidinium of CRY R446 (on α17) forms π-cation interaction with TIM Y11. TIM Y11 participates in hydrophobic contacts with CRY P257, L443 and L447. On TIM α1, TIM P8 stacks against CRY α12 and TIM S15 hydrogen bonds to the backbone carbonyl of CRY A442. (b) In the β-hairpin connecting ARM_1- α1 to ARM_1- α2 E21 salt-bridges to R474 and C19 interacts with K445. (c) Interactions of the CRY protrusion motif. TIM R109, F113, and H110 interact with the protrusion motif of CRY. TIM ARM_2-α3 H110 stacks with CRY H307. Four Met residues (M179, M181 M182, M185) in the ARM_3-α2-α3 loop provide side-chain interactions with the tip of the CRY protrusion motif. The CRY α10 helix lengthens to residue A295 compared to the dark state and the following 300-306 residues interact directly with ARM_2-α3. (d) Interactions of the CRY C-terminal lid and α20 helix. The restructured C-terminal lid interacts with residues on TIM ARM_1- α2. For examples, L34 make a hydrophobic contact with I436 and E37 hydrogen bonds to the backbone of S434. At the end of ARM_1- α2, Asn30 contacts the N-terminal end of CRY α20. A DSSO crosslink observed between Lys510 on CRY a20 and Lys41 on ARM1-α3 is fully consistent with the observed interface.

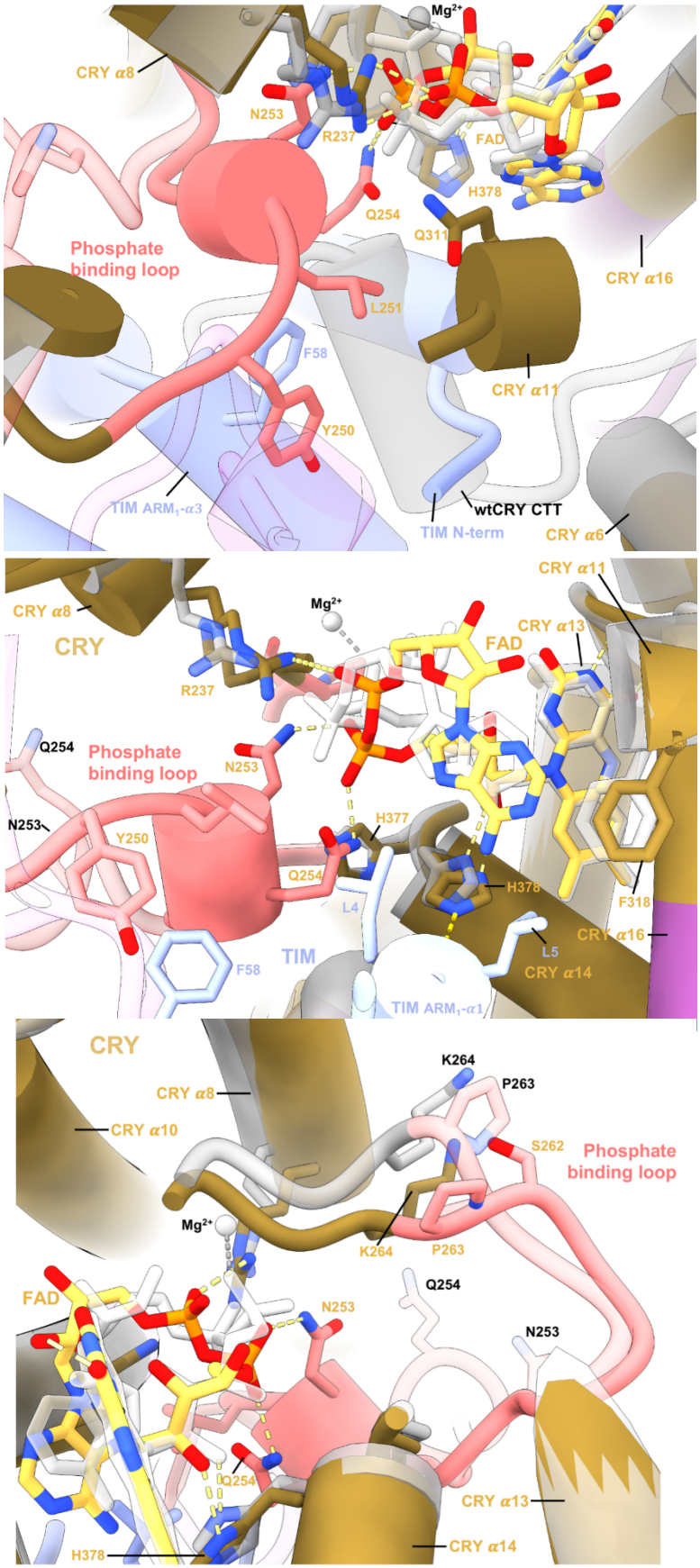

Extended Data Fig. 5

Extended Data Figure 5. Changes in flavin binding pocket for CRY dark and bound states. Comparison of the flavin pocket in CRY:TIM compared to in dark-state CRY (PDB 4GU5). (a) In CRY:TIM, Y250 and L251 interact with the FAD pocket and make space for the top of TIM ARM_1-α3 to insert F58 behind the new conformation of the phosphate-binding loop. (b) The FAD adenine ring of CRY:TIM slides 1.5 Å relative to the unbound structure. CRY F318 shifts away from its original position and harbors helix α11 to compensate for the FAD adenine ring adjustment, following the protrusion motif. (c) G311 swivels away from the inserted TIM L4. New diphosphate conformations cause rearrangement of the CRY 262-to-264 loop.

a

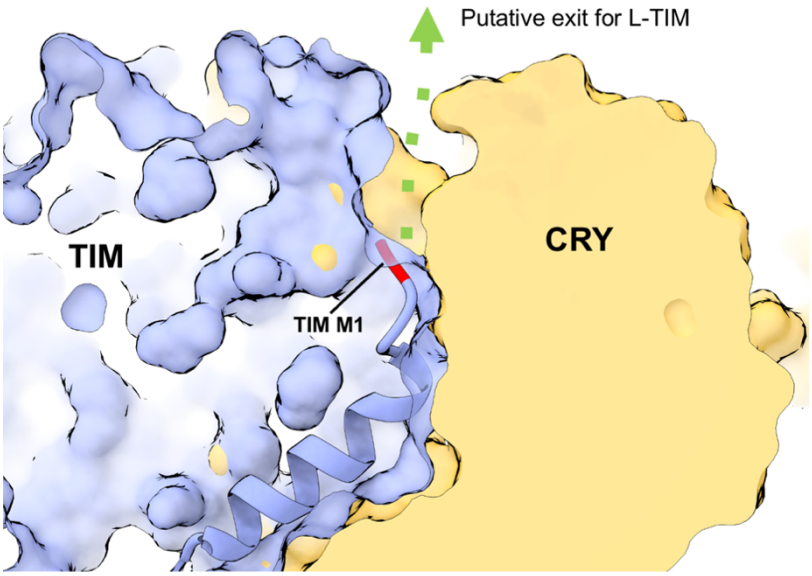

b

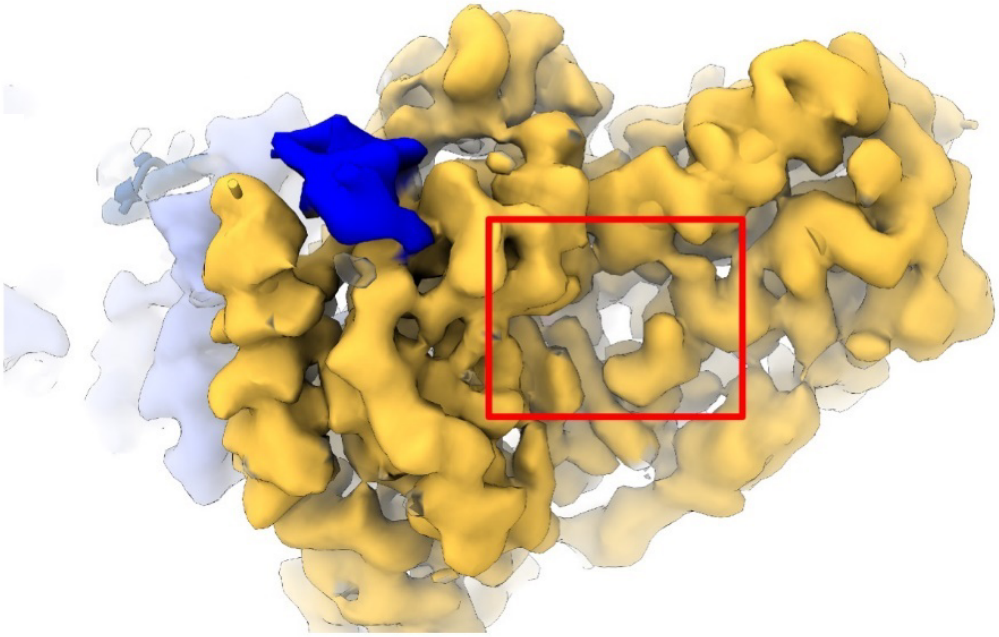

Extended Data Fig. 6

Extended Data Figure 6. Exit channel at the CRY:TIM interface and CRY secondary pocket. (a) Putative exit channel for the additional 23 N-terminal residues of L-TIM. The first residue of TIM (M1) is colored as red. A solvent accessible channel at the interface between the two proteins is marked as the green arrow. (b) Electron density for the secondary binding pocket of CRY where antenna cofactors bind in photolyases and mCRY interact with other Clock proteins (**red** box) CRY (**yellow**), TIM (**periwinkle blue**), TIM 1163-1174 (**blue**), TIM groove (**navy blue**). Although the pocket is well formed, there is no obvious density for additional moieties.

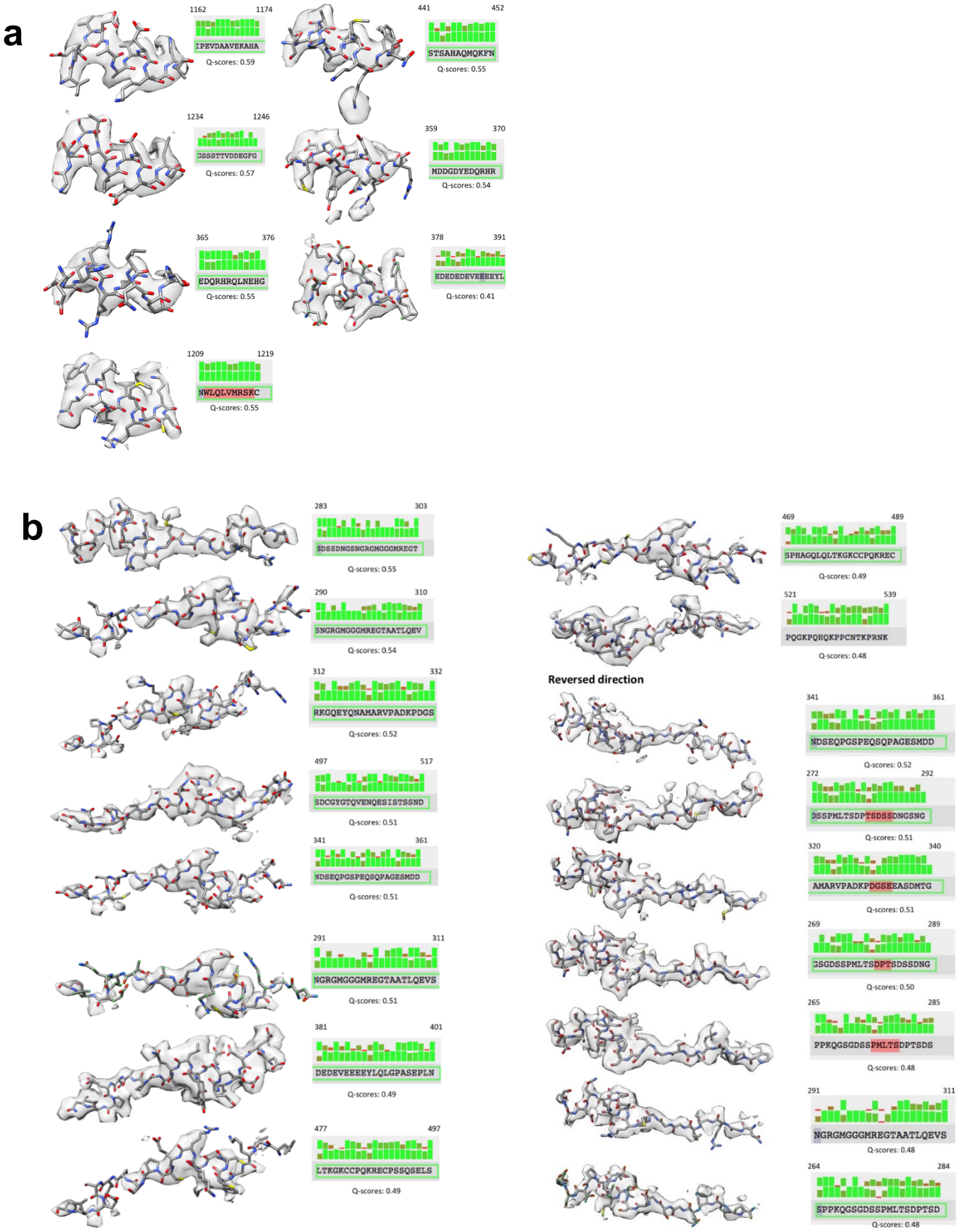

Extended Data Fig. 7

Extended Data Figure 7. TIM peripheral helix and groove peptide fitting to the electron density map and associated Q-scores. (a) Real-space electron density fitting metrics for the top scoring sequence assignments for the TIM peripheral helix. Real space density agreements were calculated in Q-scores and are shown above for sidechains and below for mainchains. (b) Real-space electron density fitting metrics for the top scoring sequence assignments for the TIM groove-binding polypeptide. Real space density agreements were calculated in Q-scores and are shown above for sidechains and below for mainchains. The TIM groove binding polypetide was tested in both directions.

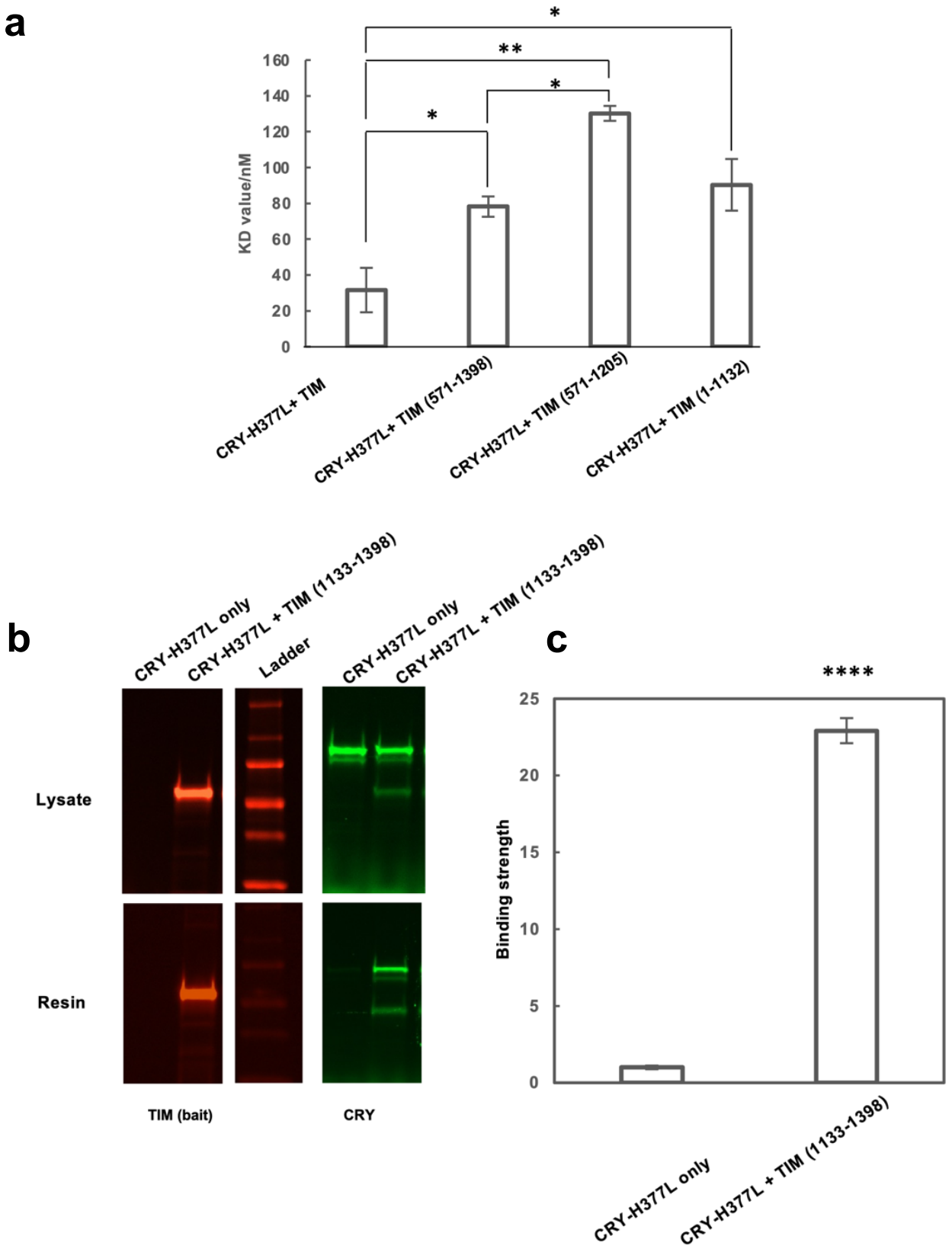

Extended Data Fig. 8

Extended Data Figure 8. Relative binding affinities between fragments of TIM and CRY H377L by the SWFTI assay. (a) The CRY H377L variant enhances binding affinity for TIM by stabilizing the TIM-binding conformation of CRY and thereby increases TIM expression levels and overall facilitates detection of weaker binding variants. sample size = 3. One-way anova was used to analyze p value. * represents $p<0.05$, ** $p<0.01$ (b) Pull down results of CRY-H377L with TIM-1133-1398. CRY-H377L interacts with the C-terminal regions of TIM. (c) Quantification of the binding strength between CRY-H377L and TIM (1133-1398) compared to the negative control (CRY-H377L only with the same amount of resin). The binding strength is defined as the amount of CRY on the resin divided by the amount of CRY in the lysate sample. The negative control is normalized to 1. Sample size = 3. Two-tailed t-test yields a p value < 0.0001 (****). Binding affinities could not be derived from this experiment owing to the challenge of producing excessive CRY relative to TIM 1133-1398.

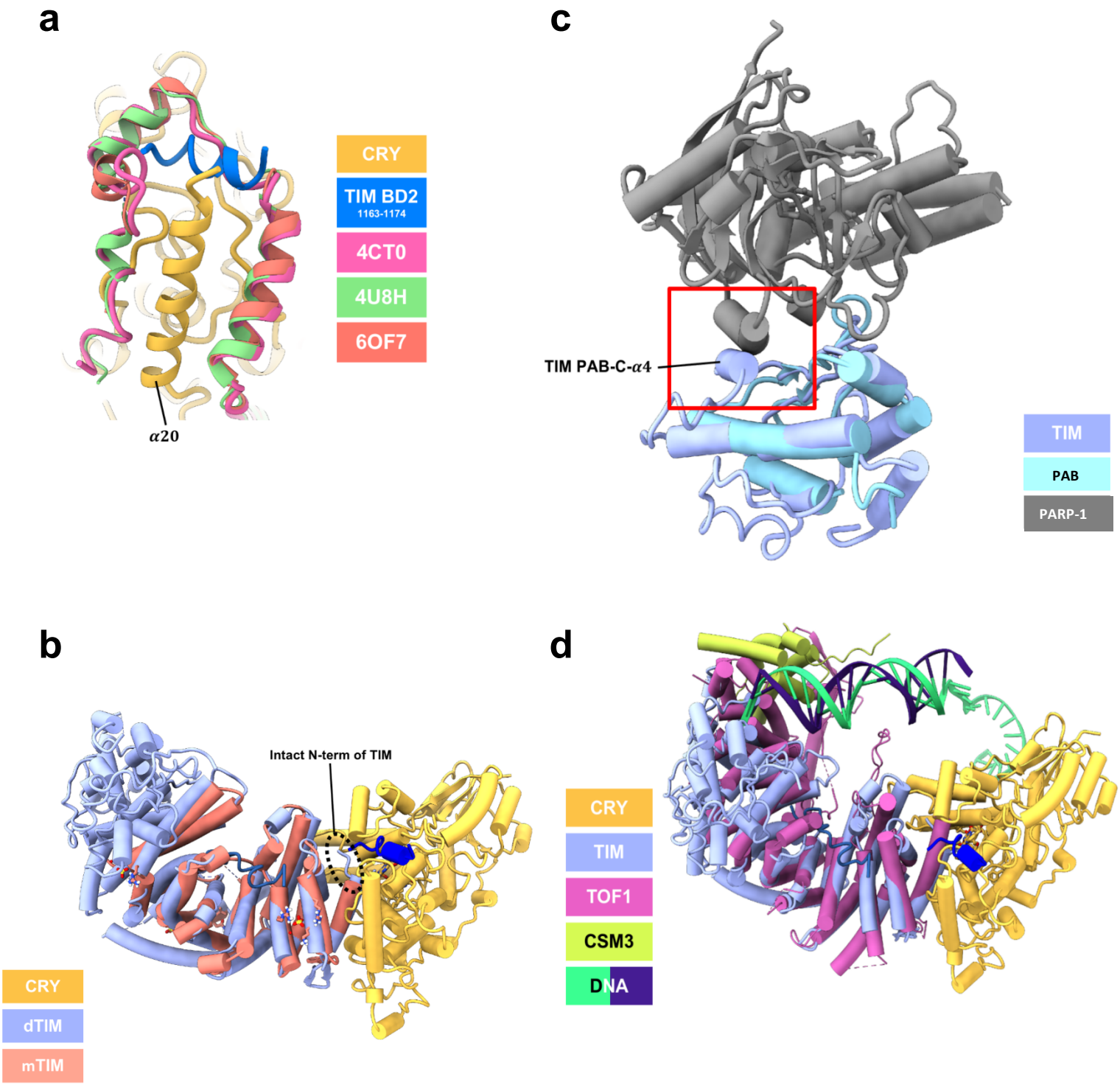

Extended Data Fig. 9

Extended Data Figure 9. Comparisons of structural features in the CRY:TIM complex to those of CRY and TIM homologues. (a) Structural comparison of CRY:TIM with mammalian CRY bound with mammalian PER. TIM 1163-1174 (**blue**) follows the backbone trace of mPER (CRYΔ (**yellow**), TIM BD2 1163-1174 (**blue**)). 4CT0: Crystal Structure of Mouse Cryptochrome1 in Complex with Period2 (**magenta**). 4U8H: Crystal Structure of Mammalian Period-Cryptochrome Complex (**green**). 6OF7: Crystal structure of the CRY1-PER2 complex (**orange red**). (b) Structural comparison of CRY:TIM (CRY (**yellow**), TIM (**periwinkle blue**), TIM 1163-1174 (**blue**), TIM groove peptide (**navy blue**)) with the crystal structure of the N-terminal domain of human Timeless (PDB ID: 5MQI, **salmon**). Note that mammalian TIM does not contain the N-terminal residues that bind into the CRY flavin pocket. (c) Structural superposition of TIM PAB (PARP-1 binding) domain with the structure of human TIM PAB bound to the PARP-1 catalytic domain. Red box highlights the TIM α-helix occupying the same space required for PARP-1 binding. TIM (this study, **periwinkle blue**), 4XHU (PAB:**sky blue**, PARP-1:**charcoal**). (d) Superposition of TIM and Tof1 within the replisome.

a

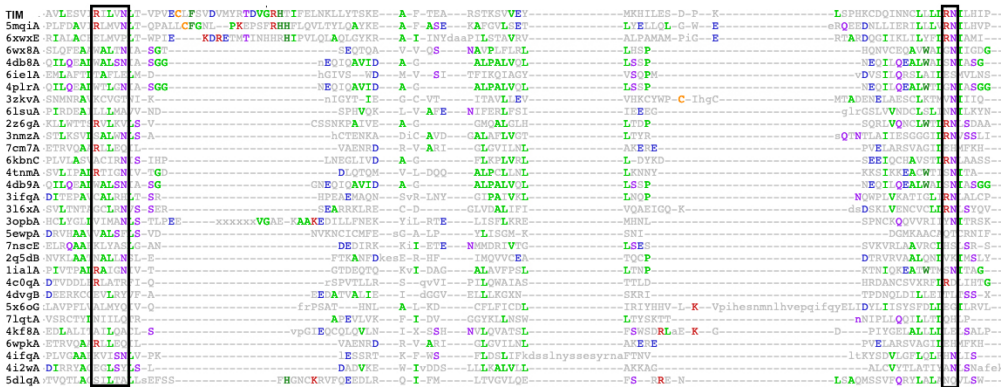

b

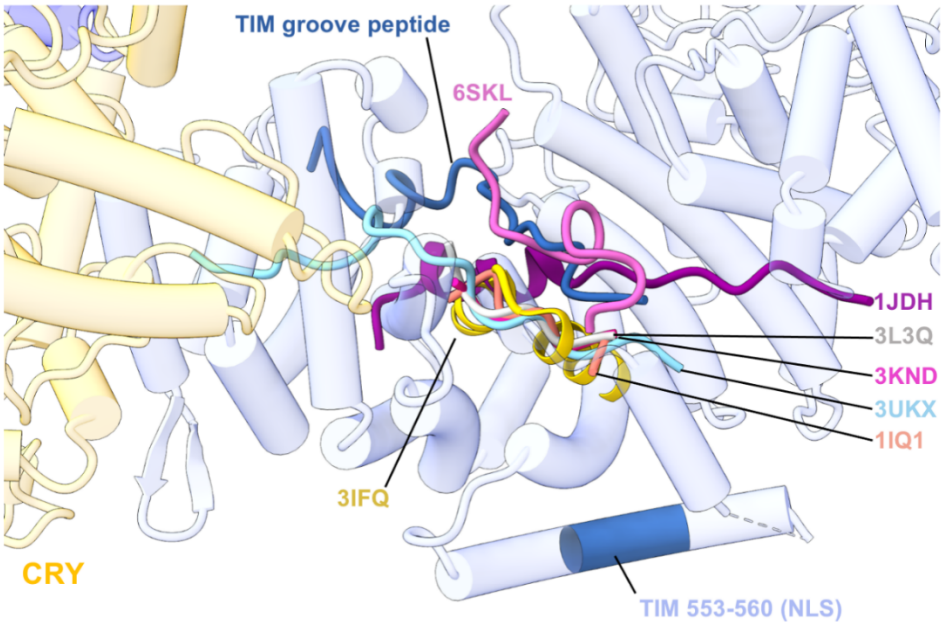

c

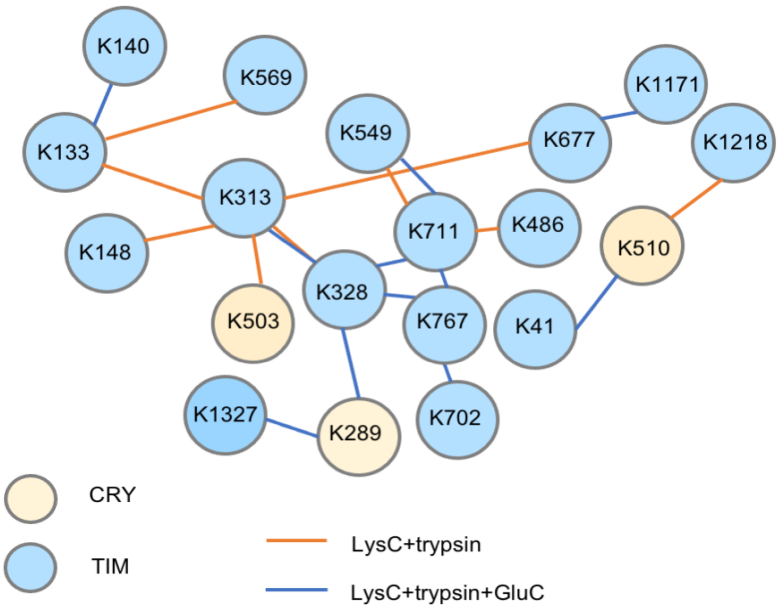

Extended Data Fig. 10

Extended Data Figure 10. Interactions between TIM and its homologs with extended polypeptides in their respective ARM grooves in relation to crosslinking map of CRY:TIM. (a) Sequence alignment of top TIM structural homologs as calculated by the DALI server[50]. Boxes outline the conserved R-XXX-N and RN residues within the ARM motifs that interact with the extended polypeptide chains of binding partners. Protein Data Bank (PDB) codes are shown on the left. (b) The extended peptide bound in the TIM groove resembles interactions found in other ARM-repeat proteins such as Importin-α1, β-catenin, and yeast TIM proteins. ARM-repeat proteins were structurally superimposed by their ARM-repeat cores to show the alignment of the extended peptides that bind in the crescent groove common to the family. For clarity only the groove peptides are displaced. Extended polypeptides found in yeast TOF1 (6SKL) and β-catenin (3IFQ) and TIM travel on the same lateral axis anti-parallel to the other importin- α, β-catenin, and TIM protein homologues. The PDB labels indicate the N-terminus of the loop. 6SKL: Cryo-EM structure of the CMG Fork Protection Complex at a replication fork - Conformation 1 (lavender), 3IFQ: Interaction of plakoglobin and β-catenin with desmosomal cadherins (**gold**), 1JDH: Crystal structure of β-catenin and htcf-4 (**purple**), 3L3Q: Mouse importin α-pepTM NLS peptide complex (gray), 3KND: TPX2:importin-αlpha complex (**magenta**), 1IQ1: Crystal structure of the importin-α(44-54)-importin-α(70-529) complex (**salmon**), 3UKX: Mouse importin-α:Bimax2 peptide complex (**sky blue**). (c) Map of DSSO lysine residue crosslinking defined by mass spectroscopy for the CRY:TIM complex. For the LysC+trypsin digested sample, although +2-charged peptides were excluded in the analysis, 59.79% sequence coverage for CRY and 49.81% for TIM were obtained. For the LysC+trypsin+GluC digested sample, 25.07% sequence coverage was obtained for CRY and 25.53% sequence coverage was obtained for TIM. Summary of the cross-links are given in the attached excel files and the raw data has been submitted to the PRIDE database.